MIT Libraries | DSpace@MIT

MIT Open Access Articles

Low-Frequency SST and Upper-Ocean Heat Content Variability in the North Atlantic

Massachusetts Institute of Technology

Low-Frequency SST and Upper-Ocean Heat Content Variability in the North Atlantic

MARTHA W. BUCKLEY AND RUI M. PONTE

Atmospheric and Environmental Research, Lexington, Massachusetts

GAËL FORGET AND PATRICK HEIMBACH

Massachusetts Institute of Technology, Cambridge, Massachusetts

ABSTRACT

A recent state estimate covering the period 1992–2010 from the Estimating the Circulation and Climate of the Ocean (ECCO) project is utilized to quantify the upper-ocean heat budget in the North Atlantic on monthly to interannual time scales (seasonal cycle removed). Three novel techniques are introduced: 1) the heat budget is integrated over the maximum climatological mixed layer depth (integral denoted as H), which gives results that are relevant for explaining SST while avoiding strong contributions from vertical diffusion and entrainment; 2) advective convergences are separated into Ekman and geostrophic parts, a technique that is successful away from ocean boundaries; and 3) air–sea heat fluxes and Ekman advection are combined into one local forcing term. The central results of our analysis are as follows: 1) In the interior of subtropical gyre, local forcing explains the majority of H variance on all time scales resolved by the ECCO estimate. 2) In the Gulf Stream region, low-frequency H anomalies are forced by geostrophic convergences and damped by air–sea heat fluxes. 3) In the interior of the subpolar gyre, diffusion and bolus transports play a leading order role in H variability, and these transports are correlated with low-frequency variability in wintertime mixed layer depths.

1. Introduction

Observations (instrumental records and proxy data) indicate that Atlantic sea surface temperatures (SSTs) exhibit significant low-frequency (intraannual–decadal) variability. Atlantic SST variability impacts regional and global climate, including temperatures across North America and Europe (Sutton and Hodson 2005; Pohlmann et al. 2006), rainfall in the Sahel region (Zhang and Delworth 2006), and frequency and intensity of Atlantic hurricanes (Knight et al. 2006; Zhang and Delworth 2006). Furthermore, knowledge of low-frequency SST variability is essential for efforts aimed at decadal climate predictions (Smith 2007; Keenlyside et al. 2008). However, the underlying causes of low-frequency SST variability are poorly understood. In particular the relative contributions of local atmospheric forcing and ocean dynamics in creating low-frequency SST anomalies

remain to be quantified. In this work, we utilize a recent state estimate from the Estimating the Circulation and Climate of the Ocean (ECCO) project to examine the relative roles of local atmospheric (wind and buoyancy) forcing and ocean dynamics in creating intraannual–interannual SST and upper-ocean heat content (UOHC) anomalies.

The "null hypothesis" for the origin of midlatitude SST anomalies is that they reflect the passive response of the ocean to stochastic atmospheric forcing. Based on the theory of stochastic climate models (Hasselmann 1976), Frankignoul and Hasselmann (1977) demonstrate that the statistical properties of observed midlatitude SST anomalies are well reproduced by the response of the ocean to stochastic air–sea heat fluxes and to a lesser extent Ekman transport anomalies (Frankignoul 1985). For example, the tripole SST anomalies seen in the North Atlantic are primarily forced by anomalous air–sea heat flux and Ekman transport anomalies associated with the North Atlantic Oscillation (NAO) (Cayan 1992a,b), and these fluxes are primarily attributable to weather noise (Fan and Schneider 2012). Frankignoul and Reynolds (1983) utilize SST and air–sea heat flux

Corresponding author address: Martha W. Buckley, Atmospheric and Environmental Research, 131 Hartwell Avenue #4, Lexington, MA 02421.
E-mail: marthabuckley@gmail.com

fields over the North Atlantic to estimate the damping parameter for SST anomalies to be $\alpha = 20\,\mathrm{W\,m^{-2}\,K^{-1}}$, which corresponds to an *e*-folding time scale of 2–6 months for mixed layer depths (MLDs) of 30–75 m. Barsugli and Battisti (1998) extend the stochastic climate model of Frankignoul and Hasselmann (1977) to include thermodynamic coupling between the atmosphere and ocean and show that in midlatitudes coupling decreases atmosphere–ocean heat fluxes and increases the variance of both SST and atmospheric temperatures at low frequencies.

In simple stochastic climate models (e.g., Frankignoul and Hasselmann 1977), the MLD must be accurately specified (as a parameter) in order to reproduce the observed magnitude of SST anomalies. More sophisticated models determine the MLD by invoking a turbulent kinetic energy budget (Niiler and Kraus 1977). Numerous studies have shown that in many regions, SST anomalies are well reproduced by forcing a one-dimensional mixed layer model with the observed atmospheric air–sea heat fluxes (e.g., Seager et al. 2000).

Despite the success of the null hypothesis in replicating SST variability in many regions, there is ample evidence that more complex dynamics play a role in creating SST anomalies in certain regions and on longer (interannual–decadal) time scales. Such SST anomalies include 1) anomalies that persist seasonally on much longer time scales than typical damping time scales and 2) low-frequency SST anomalies, particularly in regions of strong currents, that appear to be forced by ocean heat transport convergences and damped by air–sea heat fluxes. Two processes that have been hypothesized to be important in creating such SST anomalies are reemergence of SST anomalies isolated below the seasonal thermocline (essentially a one-dimensional process) and advective heat transports by ocean currents and/or planetary wave adjustments (e.g., Johnson and Marshall 2002).

Observations demonstrate that SST anomalies tend to recur from one winter to the next (e.g., Namias and Born 1970). Namias and Born (1970) hypothesize that the formation of the seasonal thermocline isolates thermal anomalies formed during wintertime convection from damping by air–sea heat fluxes. These anomalies are then reentrained the following winter when mixed layers deepen, a process that is termed the "reemergence mechanism" (Alexander and Deser 1995). Deser et al. (2003) and de Coëtlogon and Frankignoul (2003) propose an extension to the simple stochastic climate model of Frankignoul and Hasselmann (1977) that includes the effects of reemergence either implicitly by reformulating the model in terms of an effective ocean thermal capacity given by the depth of the winter mixed layer or explicitly by considering entrainment through a time-variable mixed layer. de Coëtlogon and Frankignoul (2003) demonstrate that the persistence of the tripole SST anomalies associated with the NAO may be explained through the reemergence mechanism.

While the one-dimensional processes of local atmospheric forcing and reemergence may explain SST anomalies over much of the ocean, evidence suggests that ocean advection may play a role, particularly in regions of strong currents and on decadal and longer time scales. Bjerknes (1964) and Kushnir (1994) examine relationships between Atlantic SST and sea level pressure anomalies and conclude that, while interannual SST variability is primarily driven by air–sea heat fluxes forced by atmospheric variability, ocean dynamics plays a role in setting SST on decadal time scales. Gulev et al. (2013) utilize SST and turbulent air–sea heat flux estimates to show that in the midlatitude North Atlantic surface turbulent heat fluxes are driven by the ocean on time scales longer than 10 years. The spatial pattern of decadal SST anomalies (generally a single polarity over the entire North Atlantic with maximal anomalies in subpolar regions) has led numerous authors to conclude that these anomalies are due to changes in the strength of the Atlantic meridional overturning circulation (AMOC; e.g., Kushnir 1994). Dong and Kelly (2004) and Dong et al. (2007) argue that interannual UOHC anomalies in the Gulf Stream region are forced by changes in ocean geostrophic advection and damped by air–sea heat fluxes. Marshall et al. (2001a) and Czaja and Marshall (2001) develop simple models to show that SST anomalies across the Gulf Stream path result from the delayed adjustment of the gyre circulation and/or the AMOC to stochastic wind forcing. de Coëtlogon and Frankignoul (2003) find that allowing for reemergence to occur nonlocally in accordance with estimated advection pathways leads to increased wintertime persistence, particularly in the northern portion of the North Atlantic.

The goal of this paper is to extend previous work through a refined examination of the relative contributions of local processes (atmospheric forcing and reemergence) and ocean dynamics in setting SST and UOHC on intraannual–interannual time scales. The refinement is afforded through the use of a dynamically and kinematically consistent ocean state estimate produced by the ECCO project. Two major requirements, in particular, are satisfied: 1) compared to free-running coupled or ocean-only general circulation models (GCMs), ECCO estimates are consistent (within derived uncertainty estimates) with existing ocean observations; 2) in contrast to filter-based (sequential) reanalysis products, which incur artificial heat sources/ sinks during the analysis steps, ECCO estimates are the result of a smoother-based method. As such they are

free of artificial internal heat and freshwater sources/sinks and fulfill known conservation laws exactly. This enables accurate (closed budget) term-by-term diagnostics of the heat equation.

This effort is complementary to the study of Piecuch and Ponte (2012b), which utilizes a previous ECCO estimate to demonstrate the importance of advection in setting UOHC in several broad latitude bands. Their results are extended in three important ways: 1) Advective transports resulting from local Ekman transports are isolated, allowing a separation between locally forced UOHC anomalies and ones which require active (geostrophic) ocean dynamics. 2) The dominant modes of SST and UOHC variability are considered, rather than restricting the analysis to latitude bands. 3) Rather than considering budgets over somewhat arbitrarily defined fixed-depth layers, we consider UOHC budgets integrated over the maximum climatological mixed layer depth, which reflects the portion of the ocean that comes in contact with the atmosphere.

In section 2 we introduce the current ECCO estimate, its fit to observations, and the suitability of ECCO for understanding SST and UOHC variability. In section 3 we describe the estimate's SST and UOHC variability. The roles of local atmospheric forcing (air–sea heat fluxes and Ekman transports) and ocean dynamics (primarily geostrophic advection) in setting SST and UOHC are determined in section 4. Furthermore, in section 5 the North Atlantic is divided into several dynamically distinct regions, and the important terms in the UOHC budget in each of these regions are examined. Finally, the main conclusions of our work and how they relate to previous studies are discussed in section 6.

2. The ECCO state estimate

a. Overview

In the ECCO ocean state estimation project, the Massachusetts Institute of Technology General Circulation Model (MITgcm) is fit in a least squares sense to several hundred million (satellite and in situ) ocean observations spanning the last two decades (Wunsch and Heimbach 2007; Wunsch et al. 2009). Each data point is weighted by a best estimate of its observational and representation error variance, and the least squares problem is solved by the method of Lagrange multipliers, using an iterative process relying upon a gradient search. The fit is achieved by adjusting uncertain variables (surface forcing, initial conditions, and interior mixing coefficients). The model is then run forward in time using the adjusted parameters, free of any constraints. The resulting model outputs are dynamically

and kinematically consistent: they satisfy the equations of motion and preserve property budgets exactly (Wunsch and Heimbach 2013a). Thus, ECCO estimates are particularly well suited for exploring mechanisms of SST and UOHC variability.

Through the optimization process, atmospheric forcings are adjusted (within error bars) in order to make the ECCO estimates consistent with ocean observations (also within error bars). As there are substantial uncertainties in various atmospheric data products, making adjustments within those error bars is a valid and consistent formal estimation approach. However, it is possible that the adjustments to atmospheric forcings degrade the atmospheric forcing by, for example, compensating for model errors.

As ECCO estimates are produced using an ocean-only GCM with specified (albeit adjusted) atmospheric forcing, they cannot be utilized to address the origin of atmospheric forcing. Variability in atmospheric forcing may result from internal atmospheric dynamics (Frankignoul 1985; Fan and Schneider 2012), local thermodynamic atmosphere–ocean coupling (Barsugli and Battisti 1998; Frankignoul et al. 1998), and/or dynamic atmosphere–ocean coupling (see review by Kushnir et al. 2002).

A potential disadvantage of the ECCO estimate is its relatively coarse resolution (nominally 1°). In the real ocean there may be low-frequency mesoscale variability that is not resolved by ECCO (e.g., the Gulf Stream path modulation), and parameterizations utilized to capture the effects of unresolved variability are certainly imperfect.

The new-generation ECCO version 4 (ECCO v4) estimate released by the ECCO-Production project (G. Forget et al. 2014, unpublished manuscript) covers the period 1992–2010 (with periodic updates to extend the estimation period to near present). Like in past ECCO estimates, 1992 is chosen as the beginning of the estimation period to coincide with the beginning of the satellite altimetry period for which continuous global sea level observations are available. Unlike previous ECCO estimates, the domain is global: that is, it encompasses the Arctic. A new global grid was produced to this end with slightly higher resolution, isotropic meridional scaling, refined resolution in the tropics, and grid topologies adapted to the adjoint modeling infrastructure (G. Forget et al. 2014, unpublished manuscript). Other improvements over past ECCO solutions include a state-of-the-art dynamic–thermodynamic sea ice model (Losch et al. 2010) and the use of real freshwater fluxes in conjunction with a nonlinear free surface (Campin et al. 2004). See Wunsch and Heimbach (2013a) for a summary of the observational
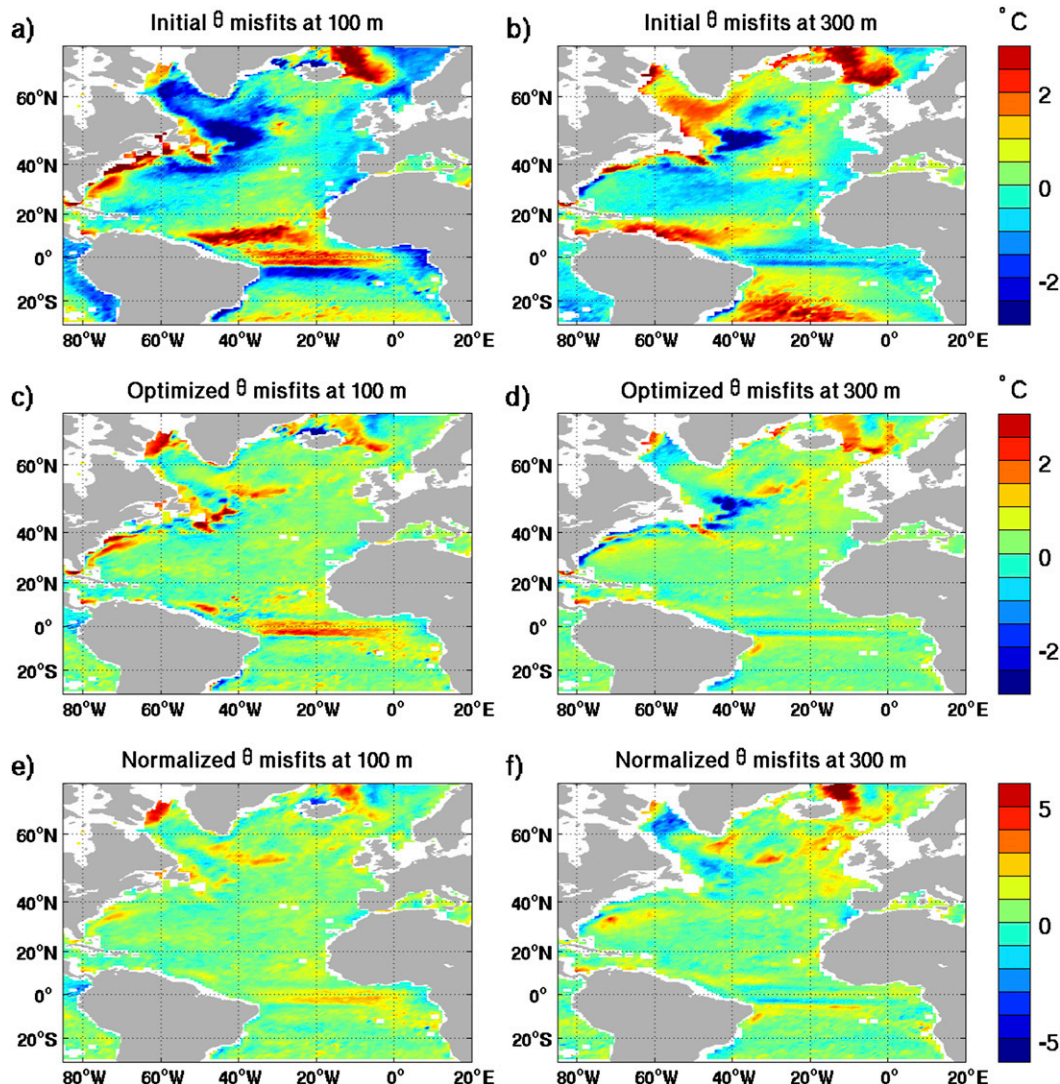
FIG. 1. (a),(b) Temperature misfits (model minus observation) for first-guess solution at (a) 100- and (b) 300-m depth for all in situ data [Argo, CTDs, XBTs, and Southern Elephant Seals as Oceanographic Samplers (SEaOS)] averaged over 1992–2010. Misfits are calculated as the sample mean for each grid cell of $\theta_e - \theta_o$, where θ_o are observational profiles and θ_e are the corresponding profiles from the model. (c),(d) As in (a),(b), but for optimized solution (ECCO v4 state estimate). (e),(f) Normalized misfits (model minus observation) for the ECCO v4 solution, calculated as the sample mean for each grid cell of $(\theta_e - \theta_o)/\theta_{sig}$, where θ_{sig} is the uncertainty (constant in time). The term θ_{sig}^2 is defined by Eq. (2) in Forget and Wunsch (2007) and θ_{sig} at 300 m is plotted in Fig. 4 in Forget and Wunsch (2007).

constraints included in this estimate and Speer and Forget (2013) for a discussion of the estimate's hydrographic properties. The specific ECCO v4 estimate discussed in this study is revision 3, iteration 3.

b. Comparison to observations

Figures 1a–d show potential temperature (θ) misfits in the upper ocean compared to in situ data for the "first guess" solution (no optimization; i.e., no adjustment of initial conditions, atmospheric forcing, or interior mixing

coefficients) and the optimized ECCO v4 solution. The first-guess atmospheric forcing is given by the European Centre for Medium-Range Weather Forecasts (ECMWF) Interim Re-Analysis (ERA-Interim) atmospheric state (surface air temperature, specific humidity, precipitation, and downwelling radiation) and wind stress vector fields. See Wunsch and Heimbach (2013a,b) and G. Forget et al. (2014, unpublished manuscript) for details regarding the data used in ECCO v4. It is clear that the optimization process has improved the fit to observations substantially,
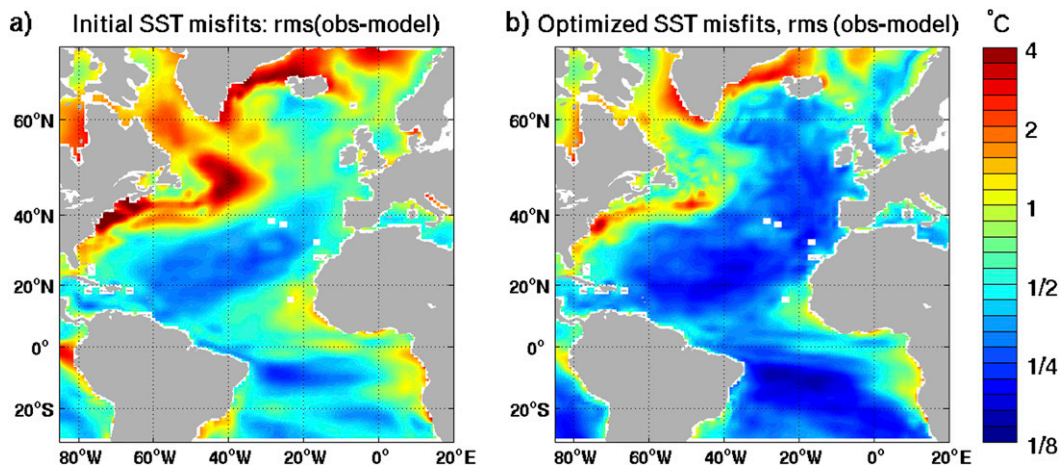
FIG. 2. Root-mean-square difference between Reynolds et al. (2002) mapped SST data and SST in (a) first-guess solution and (b) optimized solution (ECCO v4). Note the logarithmic color scale.

but errors on the order of 1°C are still present along the equator, along the Gulf Stream path, and in regions of the subpolar gyre. Normalized misfits (see Figs. 1e,f) are near one in most regions, indicating that the optimization procedure has succeeded in producing a model solution that matches observations within the observational uncertainties. Exceptions include the Greenland Sea, where normalized misfits remain significantly larger than one despite optimization, indicating a not fully converged solution in limited regions.

Figure 2 shows a map of the root-mean-square difference between Reynolds et al. (2002) mapped SST data (updated through 2010) and the first-guess solution and ECCO v4 over the Atlantic. Model–data differences are largest along the Gulf Stream path and in the area around Greenland. The root-mean-square model–data difference in space and time over the Atlantic basin is 1.0°C for the first-guess solution and 0.59°C for ECCO v4. Results presented here and ongoing model–data misfit analyses indicate that mean and time-variable upper-ocean temperatures are realistically represented in ECCO v4 and well within observation and representation error estimates. Furthermore, current ECCO estimates show only modest drifts over the 19-yr integration (G. Forget et al. 2014, unpublished manuscript; Wunsch and Heimbach 2013a).

Figure 3 shows the first two empirical orthogonal functions (EOFs) and corresponding principle component (PC) time series of anomalies of monthly (seasonal cycle removed) North Atlantic SST (1992–2010) from Reynolds data and ECCO v4. In both Reynolds data and ECCO v4, the leading two modes of variability explain ~25% and ~15% of the spatially integrated variance, respectively. The correlation between the PC time series of Reynolds data and ECCO v4 is 0.95 for both PC1 and

PC2. EOF1 resembles the classic SST tripole, which has been demonstrated to be associated with the NAO (Cayan 1992a,b), and both EOF1 and EOF2 strongly resemble the EOF patterns found by de Coëtlogon and Frankignoul (2003) (see their Fig. 5). Significant lagged correlations between PC1 and PC2 (maximum correlation of ~0.5 when PC1 leads by ~6 yr) indicate the presence of a propagating mode, although PC2 has the largest variance during the summertime (not shown), as was previously found by de Coëtlogon and Frankignoul (2003). The power spectra of the PC time series (see Fig. 3f) are red at high frequencies with slopes ranging from −1.6 to −1.8 and flatten out at a time scales between 2 and 5 years.

3. Upper-ocean heat content variability

In the remainder of this work, we examine the variability in ocean heat content between the free surface η and a fixed (in time) depth D defined by forming a monthly climatology (1992–2010) of MLD at each spatial location and choosing the maximum MLD from this monthly climatology. The heat content per unit area integrated over this layer is defined as

$$H \equiv \rho_o C_p \int_{-D}^{\eta} \theta \, dz, \tag{1}$$

where θ is temperature, ρ_o is the mean density, and C_p is the heat capacity. More common metrics of UOHC include heat content integrated over fixed depth layers (Dong and Kelly 2004; Forget 2010; Piecuch and Ponte 2012b), isothermal layers (Dong et al. 2007; Forget et al. 2011), and the mixed layer (Foltz et al. 2003; Dong and Kelly 2004; Kim et al. 2006; Foltz et al. 2013). Our novel choice for defining H is based on the following considerations:
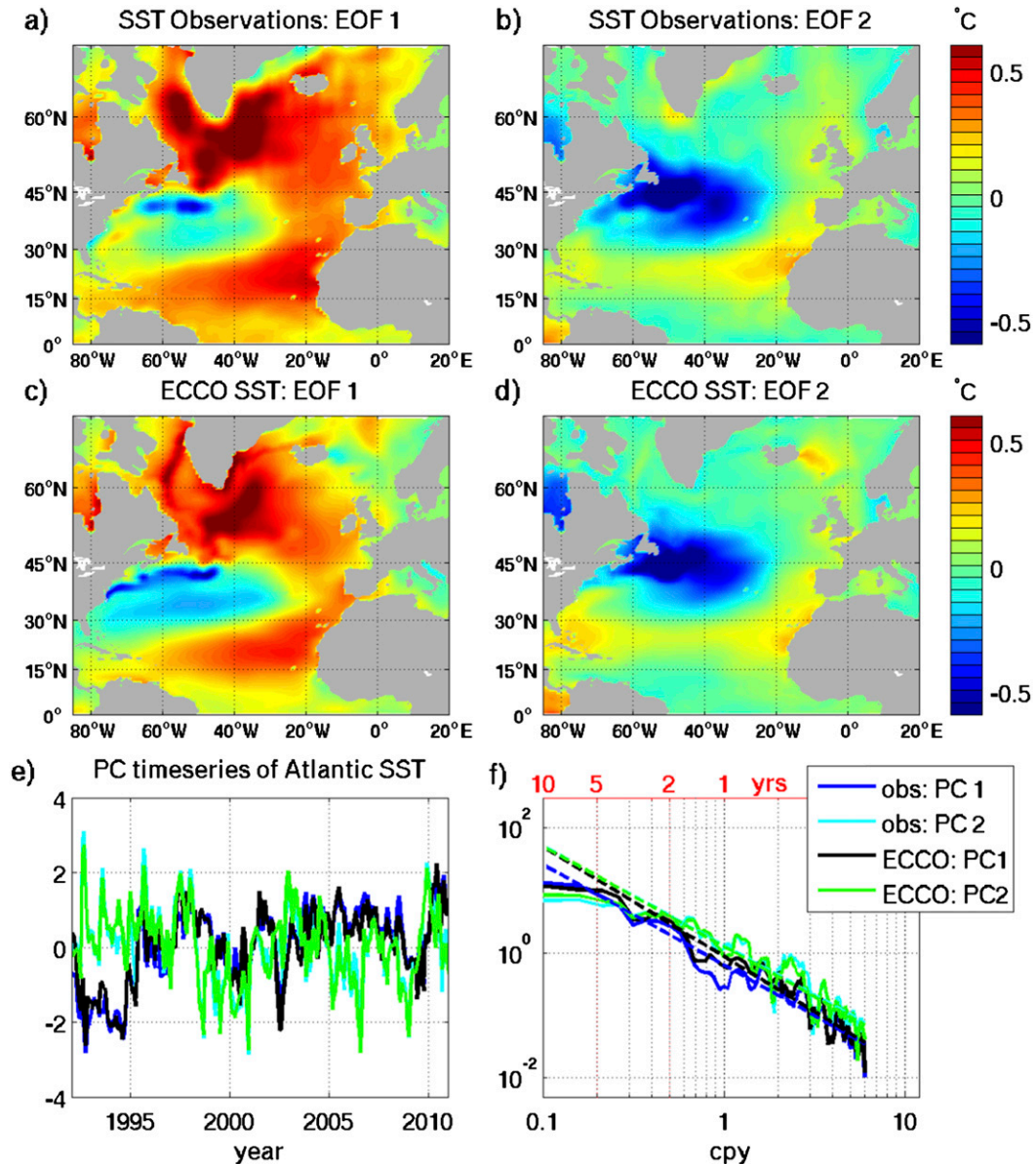
FIG. 3. (a),(b) The first two EOFs of monthly (seasonal cycle removed) North Atlantic SST anomalies from mapped Reynolds et al. (2002) data, which explain 25% and 14% of the spatially integrated variance, respectively. (c),(d) Corresponding plot for ECCO v4, for which the first two EOFs explain 24% and 15% of the spatially integrated variance, respectively. (e) The first two PC time series of North Atlantic SST from Reynolds data and from ECCO v4 and (f) respective power spectra. The dashed diagonal lines show a fit to the red portion of the power spectra ($1/6 < \tau < 5$ yr). The slope m of the fit are as follows: Reynolds PC1, $m = -1.8$; Reynolds PC2, $m = -1.6$; ECCO PC1, $m = -1.6$; and ECCO PC2, $m = -1.6$.

(i) The layer from the ocean surface to $-D$ reflects the portion of the ocean that comes in contact with the atmosphere.

(ii) Budgets from the surface to $-D$ generally do not cut across the mixed layer. When a layer budget (e.g., fixed depth layers) cuts across the mixed layer, the UOHC budget will be dominated by air–sea heat fluxes and vertical mixing (diffusion),

which redistributes heat within the mixed layer. Such a balance provides little insight into important dynamics.

(iii) Unlike budgets over the time-evolving mixed layer (e.g., Foltz et al. 2013), considering budgets over D eliminates the need to explicitly consider entrainment processes in UOHC since D is fixed in time (Deser et al. 2003).
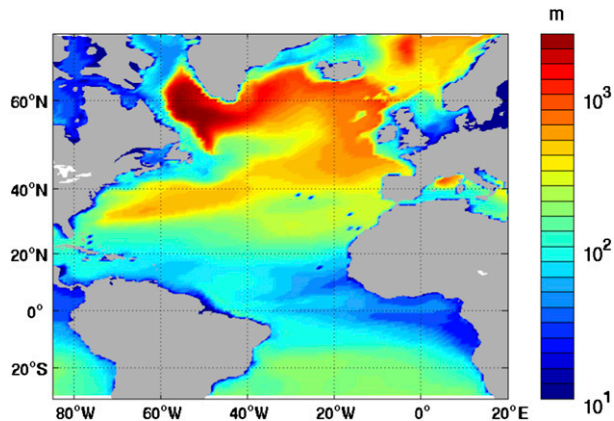
FIG. 4. The maximum climatological MLD (D) over the Atlantic basin. Note the logarithmic color scale. The MLD is defined, in accord with the criterion described in Kara et al. (2000), as the depth at which the potential density is larger than $\rho_m = \rho(1) + \alpha\Delta\theta$, where $\rho(1)$ is the potential density in the first model layer, $\Delta\theta = 0.8°C$, and $\alpha(\theta, S, p) = \partial\rho/\partial\theta$. The value of D is defined by forming a monthly climatology (1992–2010) of MLD and at each spatial location choosing the maximum MLD from this monthly climatology.

In the ECCO v4 estimate, D is deep ($\sim500\,m$) over most of the subpolar gyre, with the deepest mixed layers (greater than $1000\,m$) in the Labrador Sea (see Fig. 4). Values of D of several hundred meters are also found south of the Gulf Stream in the Eighteen Degree Water formation region (e.g., Forget et al. 2011). The shallowest mixed layers (tens of meters) occur in the tropics, particularly in the eastern portion of the basin. MLDs in ECCO compare favorably to observationally based MLD estimates using the same MLD criterion (i.e., Kara et al. 2000). For example, D values calculated from the Kara et al. (2002) MLD climatology (1900–94) are also deepest in the Labrador Sea ($>700\,m$), 100–200 m south of the Gulf Stream, and very shallow ($\sim10\,m$) in the tropics (see Fig. 13f in de Boyer Montégut et al. 2004). Different analysis periods and resolutions prevent a more quantitative comparison between ECCO and the Kara et al. (2002) MLD climatology or other available MLD climatologies.

We might alternatively choose to integrate to a depth D^*, defined as the maximum MLD at each spatial location. The variables D and D^* are only significantly different over the subpolar gyre (not shown). Integrating down to the deeper depth D^* (integral denoted H^*) is expected to further decrease the importance of vertical mixing at the expense of integrating over a layer that is only in contact with the atmosphere during "extreme" years.

In the subsequent analysis we will consider the variability of H and the terms important in the budget of H. All analyses will be conducted using monthly average

output with the seasonal cycle removed by simply subtracting the mean monthly climatology from each month. Figure 5 shows the first two EOFs and PC time series of monthly anomalies of North Atlantic H. The spatial patterns of the EOFs of H are similar to those of SST, but, as expected, the magnitude of H variability is larger in the subpolar gyre where mixed layers are deep. As with SST (Fig. 3f), the power spectra of the PC time series of H (Fig. 5b) are red at high frequencies and flatten out at low frequencies. H variability is weaker at high frequencies and stronger at low frequencies compared to that of SST (i.e., power spectra of H are steeper than those of SST) because of the integration over a deeper layer.

Figures 5e,f show SST anomalies projected[1] on to the first two PC time series of H. The patterns of SST and H are quite similar, indicating that at these low frequencies upper-ocean temperature anomalies are quite coherent with depth. Additionally, the spatial patterns of SST associated with the first two PCs of H (Figs. 5e,f) and the first two EOFs of SST (Figs. 3c,d) are quite similar, indicating the PC time series of H also capture a significant portion of low-frequency SST variance. In fact, the PC time series of SST and H are highly coherent on interannual time scales (not shown).

4. Upper-ocean heat content budgets

a. Roles of advection, diffusion, and air–sea heat fluxes

In this section, we analyze the terms that are important in the H budget. We integrate the conservation equation for heat from η to $-D$,

$$\rho_o C_p \int_{-D}^{\eta} \frac{\partial\theta}{\partial t}\,dz = -\rho_o C_p \int_{-D}^{\eta} \nabla\cdot(\mathbf{u}\theta + \mathbf{u}^*\theta)\,dz$$
$$-\rho_o C_p \int_{-D}^{\eta} \nabla\cdot\mathbf{K}\,dz + Q_{net}, \quad (2)$$

where $\mathbf{u}$ is the three-dimensional (explicit model) velocity; $\mathbf{u}^*$ is the eddy-induced transport velocity parameterized by the Gent and McWilliams (1990) scheme; $\mathbf{K}$ is the diffusive temperature flux resulting from diapycnal diffusion [convective adjustment, Gaspar et al. (1990) scheme, and background interior diffusion] and parameterized isopycnal diffusion (Redi 1982); and Q_{net} is

---

[1] Projecting a data field onto a time series means computing the covariance between the time series and the data field at each spatial location.
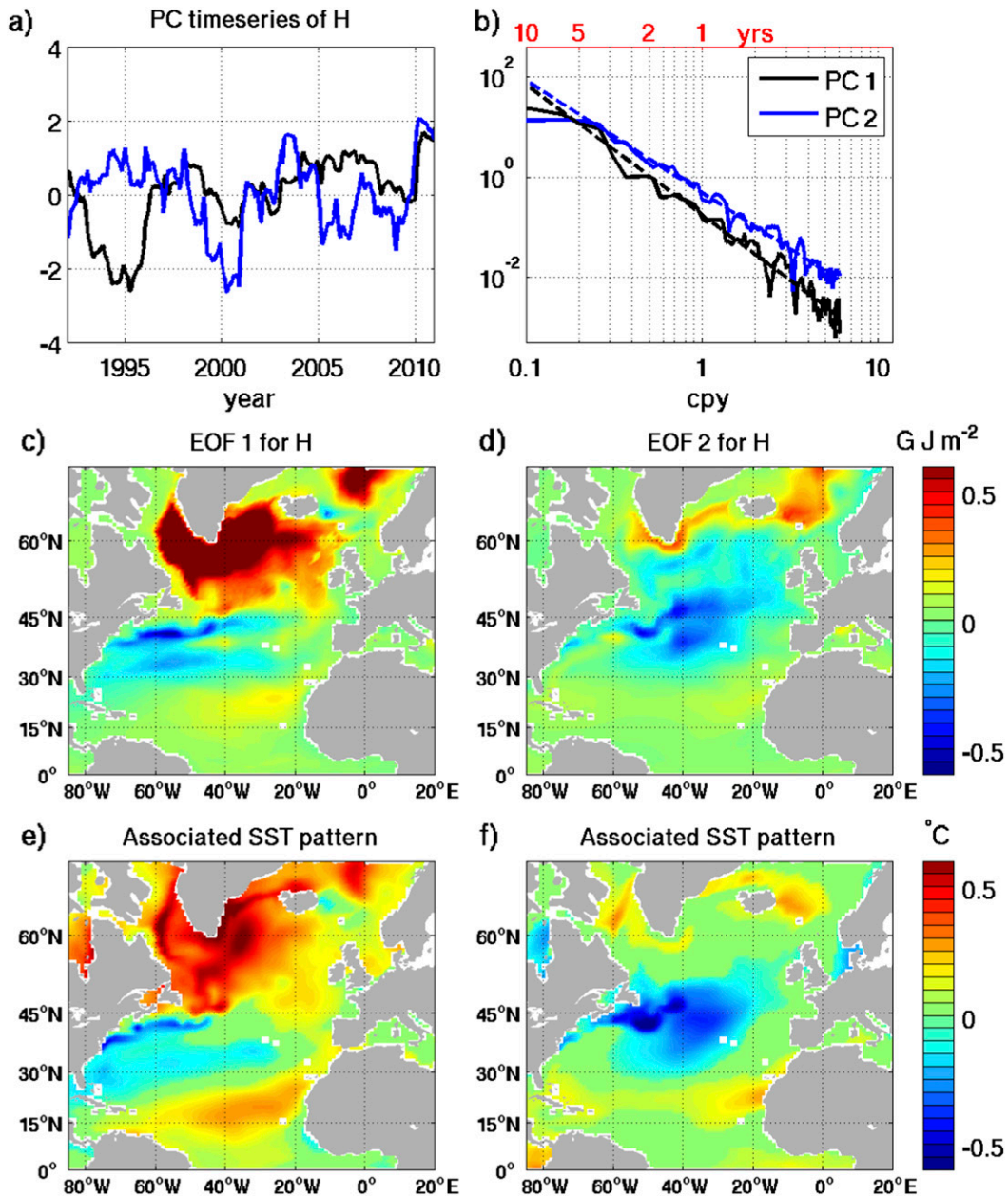
FIG. 5. (a) The first two PC time series of monthly North Atlantic heat content integrated from the surface to $-D$, denoted as H, and (b) their respective power spectra. The dashed diagonal lines show a fit to the red portion of the power spectra ($1/6 < \tau < 5$ yr). The slope m of the fit are as follows: PC1, $m = -2.6$; PC2, $m = -2.2$. (c),(d) The first two EOFs of North Atlantic H. (e),(f) The spatial patterns of SST variability associated with the first two PC time series of North Atlantic H, obtained by projecting the PC time series onto monthly SST anomalies.

the net (turbulent plus radiative) air–sea heat flux. The heat content tendency (term on the left-hand side, H_t) is given by the sum of the advective heat transport convergence (first term on right-hand side, C_{adv}), the diffusive heat transport convergence (second term on right-hand side, C_{diff}), and the air–sea heat flux less any shortwave radiation that passes through the bottom of

the climatological mixed layer (last term on right-hand side, Q_{net}).

Figure 6 shows the variance of monthly anomalies of H_t, as well as the contributions by C_{adv}, C_{diff}, and Q_{net}. The term C_{adv} plays a significant role in creating variance of H_t in regions of strong currents/fronts, such as along the Gulf Stream path. The term Q_{net} is more
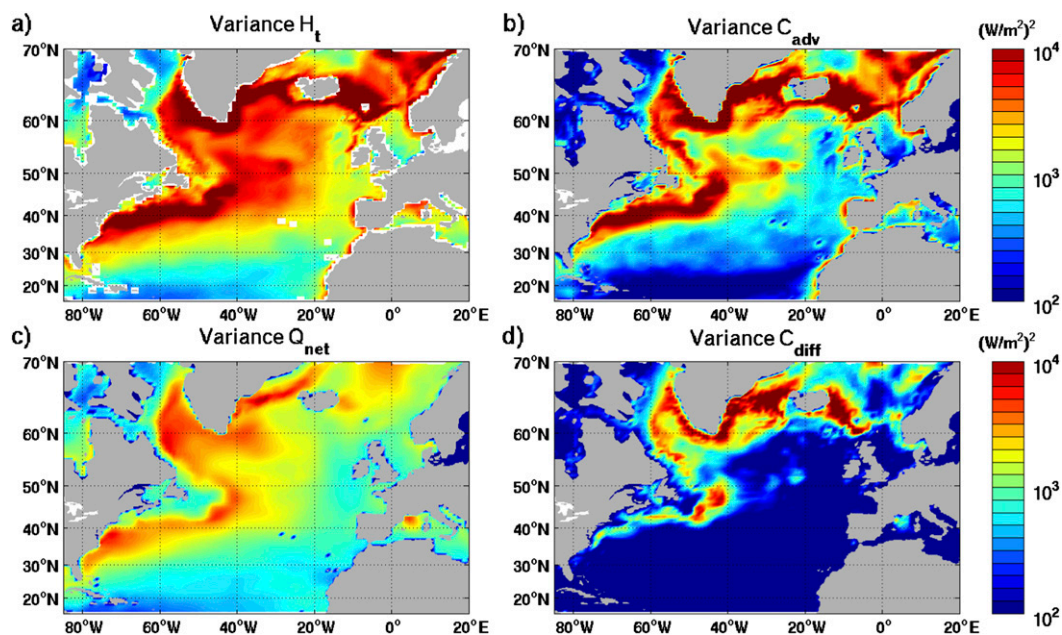
FIG. 6. Variance of monthly anomalies of the terms in the H_t budget [Eq. (2)]: (a) tendency H_t, (b) advective convergence C_{adv}, (c) air–sea heat flux Q_{net}, and (d) diffusive convergence C_{diff}. Note the logarithmic color scale.

homogenous over the entire basin than C_{adv}, but it is also largest in regions of strong currents/fronts. Consistent with the fact that our chosen layer generally does not cut across the mixed layer, C_{diff} only provides minor contributions, except over portions of the Gulf Stream (in particular the Mann eddy region centered at 45°N, 40°W) and along the boundaries in the subpolar gyre. The terms C_{adv} and Q_{net} are correlated over broad regions of the subtropical and subpolar gyres and anti-correlated over the tropics (see Fig. 7a), patterns that likely reflect the role of the winds in creating both air–sea heat flux and Ekman transport anomalies (Foltz and McPhaden 2006). The terms C_{adv} and C_{diff} are

anticorrelated over the regions where C_{diff} plays a sizable role in the H budget (see Fig. 7b).

b. Separation of advective convergence into Ekman and geostrophic parts

A primary goal of this study is to determine the dynamical mechanisms that contribute to variability of C_{adv}, specifically whether advective heat transports are attributable to the local response to surface wind stress variability (Ekman transports) or ocean dynamics (likely primarily heat transport by geostrophic currents). We first note that monthly averaged C_{adv} can be written as

$$
\begin{aligned}
C_{adv} &= -\rho_o C_p \int_{-D}^{\eta} \nabla \cdot (\overline{\mathbf{u}\theta} + \overline{\mathbf{u}^*\theta})\, dz \\
&= \underbrace{-\rho_o C_p \int_{-D}^{\eta} \nabla \cdot (\overline{\mathbf{u}}\,\overline{\theta})\, dz}_{\equiv C_{lin}} \underbrace{-\rho_o C_p \int_{-D}^{\eta} \nabla \cdot (\overline{\mathbf{u}'\theta'} + \overline{\mathbf{u}^*\theta})\, dz}_{\equiv C_{bol}} ,
\end{aligned} \tag{3}
$$

where overbars denote monthly mean variables and primes denote deviations from monthly means. The variance of the linear transport C_{lin} and the eddy-driven (bolus) transport C_{bol} are plotted in Figs. 8a,b. The variance of C_{lin} is qualitatively quite similar to that of C_{adv} (see Fig. 6b), and the correlation coefficient between monthly anomalies of C_{adv} and C_{lin} (see Fig. 9a) is

greater than 0.8 almost everywhere. Figure 9c shows the fraction of the variance of C_{adv} that is explained by C_{lin}.[2] With the exception of shallow regions (particularly in

---

[2] The fraction of the variance σ^2 of a quantity X explained by an estimate Y is given by $f = 1 - \sigma^2_{(X-Y)}/\sigma^2_X$.
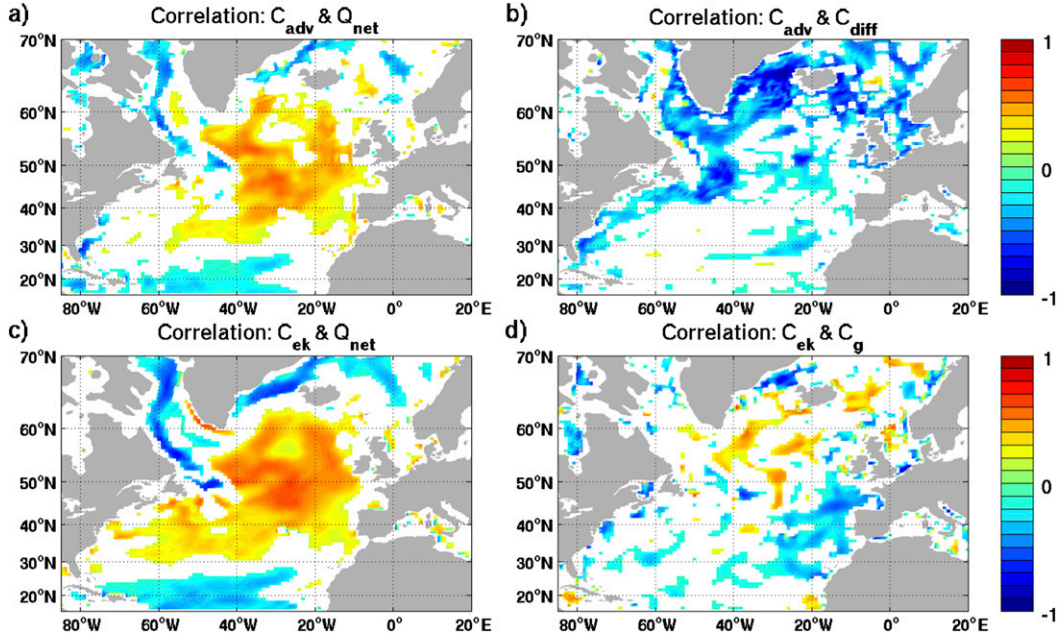
FIG. 7. Correlations between terms in the H_t budget: (a) correlation between C_{adv} and Q_{net}, (b) correlation between C_{adv} and C_{diff}, (c) correlation between Ekman convergence C_{ek} and Q_{net}, and (d) correlation between C_{ek} and geostrophic convergence C_g. Only correlations that are significant at the 95% confidence level are plotted.

the subpolar gyre) and the region of the Mann eddy, the majority of the advective heat transport convergence is captured by the linear term.

We now develop a decomposition of C_{lin} into Ekman and geostrophic parts. First, we decompose the horizontal velocity $\mathbf{u}_H$ into Ekman and geostrophic parts, $\mathbf{u}_H \approx \mathbf{u}_{ek} + \mathbf{u}_g$. Assuming that the Ekman mass transport is uniformly distributed within the Ekman layer $(-D_{ek} < z < 0)$ and zero elsewhere, the Ekman velocity is given by

$$\mathbf{u}_{ek} = \frac{\mathbf{M}_{ek}}{D_{ek}} = \frac{\boldsymbol{\tau} \times \hat{\mathbf{z}}}{\rho_o f D_{ek}}, \tag{4}$$

where $\mathbf{M}_{ek}$ is the Ekman mass transport, f is the Coriolis parameter, and $\boldsymbol{\tau}$ is the wind stress. Here, we assume that the Ekman layer is the shallower of D and a depth of 100 m [a choice motivated by the assumption that $D_{ek} = 100$ m in the Rapid Climate Change (RAPID) AMOC estimates at 26°N]. The geostrophic velocity is given by

$$\mathbf{u}_g = \frac{1}{f \rho_o} \hat{\mathbf{z}} \times \boldsymbol{\nabla} p, \tag{5}$$

where p is the hydrostatic pressure. We then integrate the continuity equation from η to $-D$ to approximate the vertical velocity at $z = -D$,

$$w(-D) = \frac{d\eta}{dt} + (E - P - R) + \int_{-D}^{\eta} \boldsymbol{\nabla}_H \cdot \mathbf{u} \, dz$$

$$\approx \underbrace{\int_{-D}^{\eta} \boldsymbol{\nabla}_H \cdot \mathbf{u}_{ek} \, dz}_{\equiv w_{ek}(-D)} + \underbrace{\int_{-D}^{\eta} \boldsymbol{\nabla}_H \cdot \mathbf{u}_g \, dz}_{\equiv w_g(-D)}, \tag{6}$$

where E, P, and R are the evaporation, precipitation, and runoff fields, respectively. Here, the terms $E - P - R$ and $d\eta/dt$ are found to be two orders of magnitude smaller than the horizontal divergence and are thus neglected. The Ekman and geostrophic components of C_{lin} are approximated as

$$C_{ek} = -\rho_o C_p \int_{-D_{ek}}^{\eta} \boldsymbol{\nabla} \cdot (\overline{\mathbf{u}}_{ek} \overline{\theta}) \, dz$$

$$+ \rho_o C_p \overline{w}_{ek}(-D) \overline{\theta}(-D) \tag{7}$$

and

$$C_g = -\rho_o C_p \int_{-D}^{\eta} \boldsymbol{\nabla} \cdot (\overline{\mathbf{u}}_g \overline{\theta}) \, dz + \rho_o C_p \overline{w}_g(-D) \overline{\theta}(-D), \tag{8}$$

where $\overline{\mathbf{u}}_{ek}$ and $\overline{\mathbf{u}}_g$ are given by Eqs. (4) and (5), respectively, and $\overline{w}_{ek}(-D)$ and $\overline{w}_g(-D)$ are given by Eq. (6).
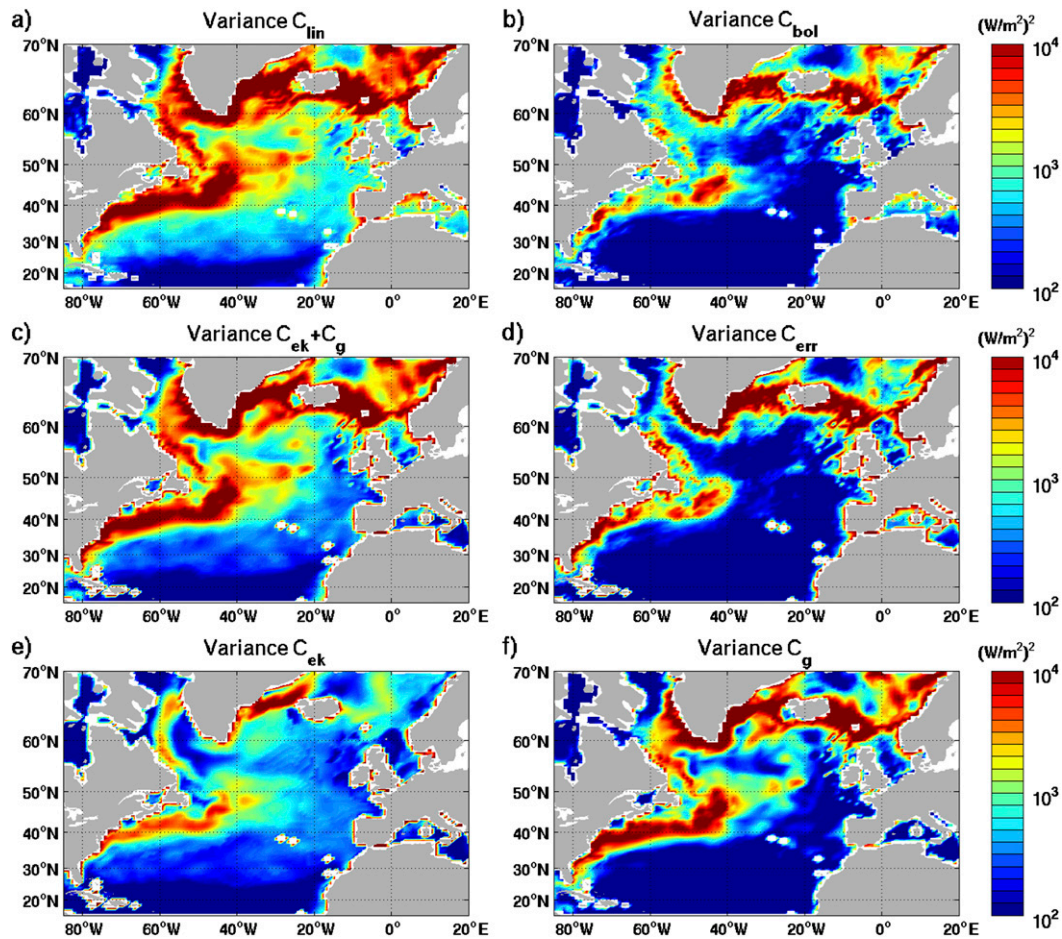
FIG. 8. Variance of monthly anomalies of the components of C_{adv}: (a) C_{lin}, (b) C_{bol}, (c) $C_{ek} + C_g$, (d) $C_{err} = C_{lin} - (C_{ek} + C_g)$, (e) C_{ek}, and (f) C_g. Note the logarithmic color scale.

Figure 8c shows the variance of our estimate of the linear heat transport convergence $C_{ek} + C_g$, and Fig. 8d shows the variance of the error introduced by this estimation $C_{err} = C_{lin} - (C_{ek} + C_g)$. The variance of $C_{ek} + C_g$ is qualitatively quite similar to that of C_{lin} (see Fig. 8a), and $C_{err} \ll C_{ek} + C_g$, except in a few shallow regions along the ocean boundaries. Physical reasons why C_{err} is large in shallow boundary regions include our neglect of inertia and viscous processes (lateral friction and bottom Ekman layers). The term C_{err} may also be large in these regions for numerical reasons; for example, errors are induced in the calculation of $\mathbf{u}_g = (u_g, v_g)$ near boundaries because on a C grid $\partial p/\partial x$ is at u points and must be interpolated onto v points to calculate v_g (and similarly for the calculation of u_g). Correlations between C_{lin} and $C_{ek} + C_g$ (see Fig. 9b) are greater than 0.8, and the fraction of the variance of C_{lin} explained by $C_{ek} + C_g$ (see Fig. 9d) is greater than 0.7 everywhere except shallow boundary regions. In summary, with the exception of shallow coastal regions, C_{lin} is well reproduced by $C_{ek} + C_g$, and our decomposition into Ekman and geostrophic components provides useful insight into the origin of the linear advective heat transport convergences observed in ECCO.

Variance maps of C_{ek} and C_g (see Figs. 8e,f) exhibit their largest values in regions of strong currents/fronts. Both strong geostrophic currents and large temperature gradients contribute to large values of C_g in these regions. While Ekman mass transports are more homogenous over the basin (not shown), C_{ek} is also large over these regions because of strong temperature gradients. Unlike C_g, C_{ek} also exhibits significant variability over the interior of the gyres.

The calculation of C_{ek} is relatively insensitive to the assumed depth of the mixed layer D_{ek}; taking $D_{ek} = 50$ m instead of 100 m results in negligible changes in C_{ek} (not shown). Since $\mathbf{u}_{ek}$ is constant over D_{ek}, the first term in the equation for C_{ek} [Eq. (7)] can be written as (neglecting small horizontal variations in η)
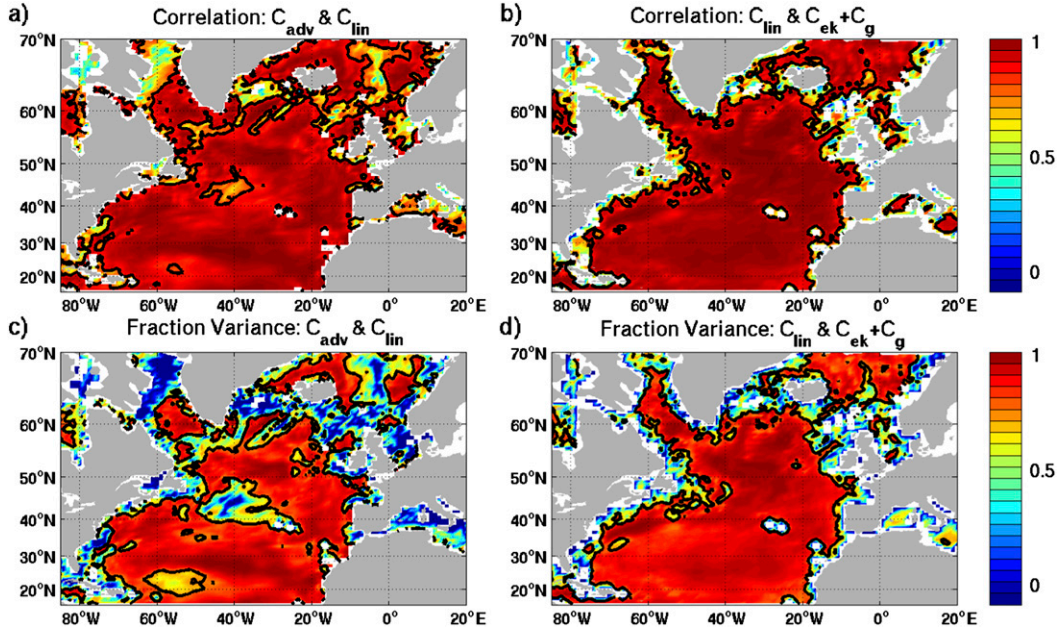
FIG. 9. Maps showing the correlation coefficient (at each spatial location) (a) between C_{adv} and C_{lin} and (b) between C_{lin} and $C_{\mathrm{ek}} + C_g$. Only correlations that are significant at the 95% confidence level are plotted. The heavy black contours indicate a correlation of 0.8. Maps showing the fraction of the variance (at each spatial location) of (c) C_{adv} explained by C_{lin} and (d) C_{lin} explained by $C_{\mathrm{ek}} + C_g$. The heavy black contours are where the fraction of the variance is equal to 0.7.

$$-\rho_o C_p \nabla \cdot (\overline{\mathbf{M}}_{\mathrm{ek}}[\overline{\theta}]),$$

where $[\overline{\theta}]$ is $\overline{\theta}$ averaged over the Ekman layer. The second term in the Equation for C_{ek} is independent of D_{ek}. Hence, the value of D_{ek} only determines the depth over which the temperature is averaged, which explains the relative insensitivity of the calculation to D_{ek}.

The correlation patterns between C_{ek} and Q_{net} (Fig. 7c) are quite similar to the correlation patterns between C_{adv} and Q_{net} (Fig. 7a). These correlation patterns are consistent with the hypothesis that changes in the wind stress lead to changes in both Q_{net} and C_{ek}, a result that was previously found by Foltz and McPhaden (2006) in the tropics. For example, a positive phase of the NAO leads to negative Q_{net} in the tropics and subpolar regions and positive Q_{net} in the subtropics and northward Ekman transport anomalies (hence $C_{\mathrm{ek}} > 0$) in the tropics/subtropics and southward Ekman transport anomalies (hence $C_{\mathrm{ek}} < 0$) in the subpolar regions (Cayan 1992a,b; Marshall et al. 2001b). The resulting correlation patterns are negative in the tropics and positive in the subtropics and subpolar regions, as observed. If alternatively, as a reviewer suggested, changes in C_{ek} forced SST anomalies that were then damped by air–sea heat fluxes, C_{ek} and Q_{net} would be anticorrelated

everywhere. Correlations between C_{ek} and C_g (see Fig. 7d) and between Q_{net} and C_g (not shown) are generally small and without clear spatial structure.

The fraction of the variance of H_t explained by our decomposition is summarized in the top panels of Fig. 10. Figure 10a shows the fraction of the variance of H_t explained by $C_{\mathrm{lin}} + Q_{\mathrm{net}}$. Regions where this quantity is not approximately 1, such as shallow subpolar regions and the region of the Mann eddy, highlight areas where diffusion and bolus transports are important in the heat budget. Figure 10b shows the fraction of the variance of H_t explained by $C_{\mathrm{ek}} + C_g + Q_{\mathrm{net}}$. The similarity between Figs. 10a and 10b indicates that approximating the linear convergence as the sum of the Ekman and geostrophic parts does not lead to substantial errors in the budget for H_t. The areas where the fraction of the variance of H_t explained by $C_{\mathrm{ek}} + C_g + Q_{\mathrm{net}}$ is approximately 1 are the regions where we can understand the majority of the variance of H_t by utilizing our decomposition of the heat transport convergence into Ekman and geostrophic parts.

To our knowledge, no author has previously utilized a decomposition into Ekman and geostrophic heat transport convergences that includes the vertical terms, as we have done here. However, a number of other studies have utilized similar decompositions. Marshall et al.
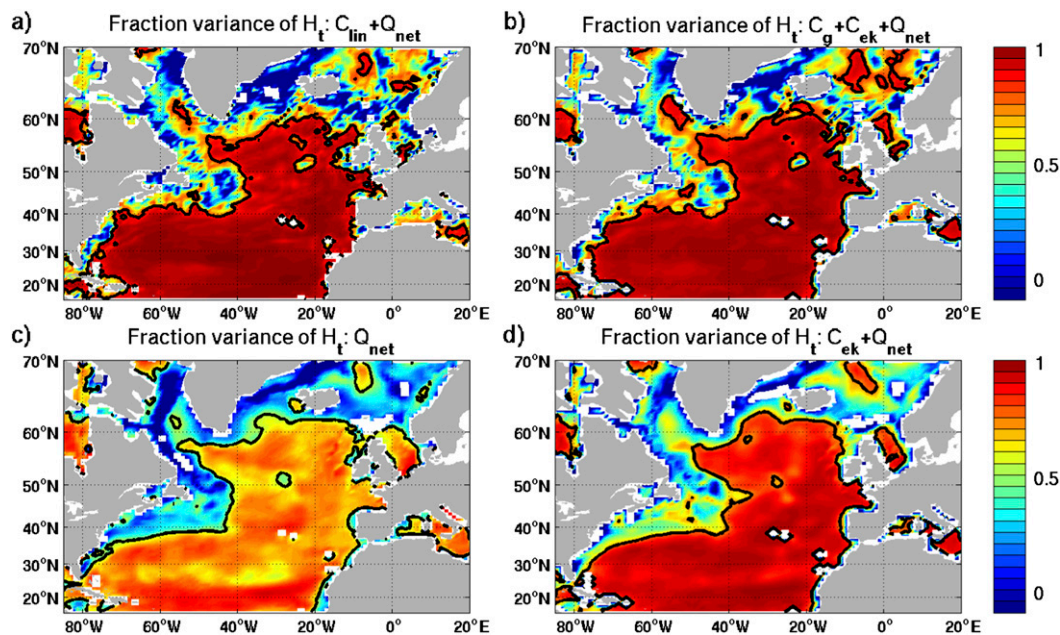
FIG. 10. Maps showing the fraction of the variance of H_t explained by (a) $C_{lin} + Q_{net}$, (b) $C_{ek} + C_g + Q_{net}$, (c) Q_{net}, and (d) local atmospheric forcing $C_{loc} = C_{ek} + Q_{net}$. Black contours are at levels of 0.7 in (a),(b),(d) and 0.5 in (c).

(2001a) express the Ekman heat transport convergence as a pseudo air–sea heat flux $H_{ek} = C_p \rho_o D_{ek} \mathbf{u}_{ek} \cdot \nabla \text{SST}$, which is equivalent to our definition of the Ekman heat transport convergence if 1) we integrate over the full ocean depth so that the vertical term disappears, 2) we assume that the mean temperature over the depth of the Ekman layer is the same as the SST, and 3) $\theta \nabla \cdot \mathbf{u}_{ek} \ll \mathbf{u}_{ek} \cdot \nabla \theta$ so that $\nabla \cdot (\mathbf{u}_{ek}\theta) \approx \mathbf{u}_{ek} \cdot \nabla \theta$. Additionally, a number of authors have calculated the (depth integrated) meridional ocean heat transport (OHT) convergence resulting from Ekman transports (Levitus 1987; Jayne and Marotzke 2001), and the RAPID program utilizes a decomposition of the AMOC and OHT into Ekman and geostrophic parts in order to estimate their strengths at 26.5°N (Cunningham et al. 2007; Johns et al. 2011).

c. Role of local forcing

As stated earlier, a primary goal of this work is to determine the relative roles of local atmospheric forcing and ocean dynamics in setting H_t. Here, local atmospheric forcing is defined simply as the sum of the air–sea heat fluxes and Ekman heat transport convergences ($C_{loc} \equiv Q_{net} + C_{ek}$). Our definition of C_{loc} is motivated by an attempt to determine in what regions and on what time scales geostrophic ocean currents can be neglected as a source of variability of H_t. Furthermore, if C_{ek} is primarily driven by changes in Ekman mass transports attributable to local wind variability rather than changes

in the temperature field (Doney et al. 2007), C_{loc} can be estimated directly from local atmospheric forcing fields. Since ECCO is an ocean-only model, we cannot address the origin of the atmospheric forcing: specifically, whether the ocean plays a role in variability of air–sea fluxes of heat, momentum, and freshwater (here called the atmospheric forcing). However, previous work (Kushnir et al. 2002; Schneider and Fan 2012) demonstrates that the response of the extratropical atmosphere to midlatitude SST anomalies is relatively small compared to internal atmospheric variability, so much of the variability of C_{loc} likely reflects stochastic atmospheric forcing.

Figure 10c shows the fraction of the variance of H_t explained by Q_{net}. As expected, because of large advective heat transport convergences over the Gulf Stream and other boundary current regions, air–sea heat fluxes cannot explain H_t over these regions. However, even in the interior of the subtropical and subpolar gyres, Q_{net} only explains on the order of 50% of the variance of H_t. Figure 10d shows the percent of the variance of H_t explained by C_{loc}. Over the interior of the subtropical and eastern subpolar gyres, over 70% of the variance of H_t is explained by local forcing. Thus, when attempting to isolate the role of local atmospheric forcing in creating H_t anomalies, Ekman heat transport convergences should be included in addition to air–sea heat fluxes, which are traditionally used as the measure of the role of local forcing.
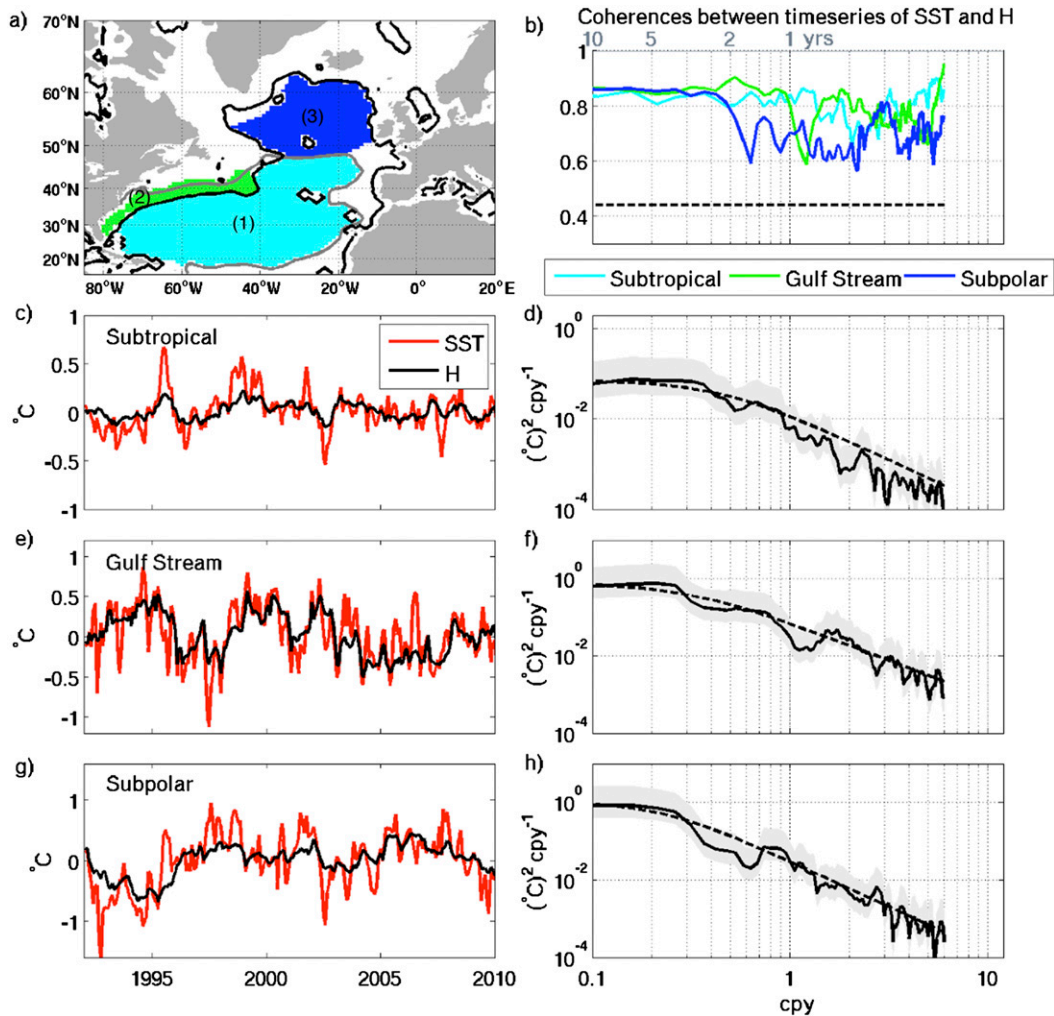
FIG. 11. (a) The three regions of the North Atlantic for which we consider H budgets: 1) the interior of the subtropical gyre, 2) the Gulf Stream, and 3) the interior of the subpolar gyre. The boundary between the subtropical and subpolar gyres is determined by the zero contour of the mean barotropic streamfunction (gray contour). The interior of the subtropical and subpolar gyres are determined by requiring that C_{loc} explains at least 70% of the variance of H_t (inside black contour) and the MLD is less than 1000 m. The Gulf Stream region is defined where the mean current speed is greater than 7 cm s^{-1}, the latitude is between 25° and 45°N, and C_{loc} explains less than 70% of the variance of H_t (outside black contour). Time series of SST and H averaged over (c) interior of the subtropical gyre, (e) Gulf Stream region, and (g) interior of the subpolar gyre. Power spectra (black lines with uncertainty indicated by gray shading) of H in (d) interior of the subtropical gyre, (f) Gulf Stream region, and (g) interior of the subpolar gyre. The dashed black lines show a fit of Eq. (10) to the spectra. (b) Coherence between time series of SST and H in each region.

5. Regional analysis of H variability

We now consider H budgets over various regions in more detail. Gyre-scale regions are chosen in accord with the large-scale nature of the dominant modes of SST and H variability (see EOFs of SST and H in Figs. 3 and 5) and the relatively homogenous values of the fraction of the variance explained by local forcing over broad regions (values near 0.7 in the interior of the subtropical and subpolar gyres and values on the order of 0.5 over the Gulf Stream region). The regions

considered are 1) the interior of the subtropical gyre, 2) the Gulf Stream, and 3) the interior of the eastern subpolar gyre (see Fig. 11a and associated figure caption for the specific region definitions). The zero contour of the mean barotropic streamfunction separates the subtropical and subpolar gyres, and the Gulf Stream region is defined by requiring mean current speeds to be greater than 7 cm s^{-1}. Gyre interiors are defined (somewhat unconventionally) by requiring that C_{loc} explains at least 70% of the variance of H_t, a choice made in order to define regions where similar dynamics play a role in the

heat budget. Time series of SST and H in each region (see Figs. 11c,e,g) are highly coherent on time scales longer than about 2 years (see Fig. 11b). The power spectra of H in each region are red at high frequencies and flatten out at low frequencies (see Figs. 11d,f,h).

Here, we focus on three regions where diffusion and bolus transports do not play a significant role in the variance of H_t. In these regions we can separate the roles of local atmospheric forcing (air–sea heat fluxes and Ekman transport convergences) and ocean dynamics (geostrophic transports) in creating H anomalies. However, the regions where these simple ideas fail are also interesting. In particular, the Mann eddy region has been isolated as a region where diffusion and bolus transports play a significant role in the heat budget. This region certainly deserves more study, in particular because previous work has suggested that this region is important for controlling variability of the AMOC (Forget et al. 2008a,b; Buckley et al. 2012; Tulloch and Marshall 2012).

a. Heat budgets over regions

The left panels of Fig. 12 show the power spectra of the terms of the H_t budget in each region. In all regions the spectra of Q_{net} and C_{ek} (and hence C_{loc}) are essentially white, consistent with the hypothesis that they are driven by local wind forcing, whereas C_g and $C_{diff} + C_{bol}$ have red spectra. Everywhere, C_{err} is small, although in the Gulf Stream region C_{err} exhibits increased variance at low frequencies. The right panels of Fig. 12 show the magnitude of the coherence between H_t and Q_{net}, C_{loc}, and $C_{loc} + C_g$ in each region. The salient message is that in the interior of the subtropical gyre local atmospheric forcing explains the majority of the variability of H_t on all time scales. In contrast, in the Gulf Stream region, C_g plays a role in H_t variability for periods longer than about 1 yr. In the subpolar gyre both C_g and $C_{diff} + C_{bol}$ are important in setting H_t for periods longer than about 2 years.

To better understand the significant low-frequency variability of $C_{diff} + C_{bol}$ in the subpolar gyre, yearly average time series of C_{diff}, C_{bol}, and their sum are compared to a time series of the March MLD averaged over the subpolar gyre (see Fig. 13). March MLD is several hundred meters deeper than D (dashed red line in Fig. 13) for 1992–95 and generally somewhat shallower than D after 1996. The time series of C_{diff} and C_{bol} are highly correlated with March MLD: during years with deeper winter mixed layers, warming of the layer by C_{diff} and C_{bol} is larger. The horizontal contribution to C_{diff} dominates over the vertical contribution (not shown), suggesting that the correlation between C_{diff} and March MLD is attributable to lateral diffusion restratifying a newly formed mixed layer rather than

vertical mixing resulting from convective instability (although this term does play a role when MLD variations are large). The correlation with C_{bol} is likely the result of increased stirring by the Gent and McWilliams (1990) scheme when isopycnal slopes increase.

To determine which terms play the largest role in creating H anomalies, we now consider time-integrated budgets. As the volume of each region is quite different, instead of considering the heat content, which will depend on the volume of the box, we choose to consider budgets of the average temperature over the layer from the surface to $-D$, $\theta = H(\rho_o C_p V)^{-1}$, where V is the volume of the box. Dividing Eq. (2) for the H budget by $\rho_o C_p V$ and integrating in time yields

$$\underbrace{\int_0^t \frac{H_t}{\rho_o C_p V} dt}_{\equiv (\theta - \theta_o)} = \underbrace{\int_0^t \frac{C_{adv}}{\rho_o C_p V} dt}_{\equiv \theta_{adv}} + \underbrace{\int_0^t \frac{C_{diff}}{\rho_o C_p V} dt}_{\equiv \theta_{diff}}$$
$$+ \underbrace{\int_0^t \frac{Q_{net}}{\rho_o C_p V} dt}_{\equiv \theta_Q} . \tag{9}$$

Similarly, we divide the equations for C_{lin}, C_{bol}, C_g, C_{ek}, C_{err}, and C_{loc} by $\rho_o C_p V$ and integrate in time to yield θ_{lin}, θ_{bol}, θ_g, θ_{ek}, θ_{err}, and θ_{loc}, respectively.

The left panels of Fig. 14 show time series of the terms in the θ budget in each of the three regions. As the quantities plotted are cumulative sums of fluxes, they start at zero. Since the mean monthly climatology has been subtracted from the fluxes, the cumulative sums tend to come back to near zero at the end of the time series (although this is not a constraint). Since budgets for $\theta - \theta_o$ are computed by cumulatively summing fluxes, there is the potential that any errors introduced by approximating $\theta_{lin} \approx \theta_{ek} + \theta_g$ will accumulate with time. However, $\theta_{err} = \theta_{lin} - \theta_{ek} - \theta_g$ is entirely negligible in the subtropical and subpolar gyres. In the Gulf Stream region, θ_{err} is small but not entirely negligible, particularly on longer time scales. The terms θ_{err} and $\theta_{bol} + \theta_{diff}$ are highly anticorrelated (correlation is -0.90), which seems to suggest that θ_{err} reflects physical processes, such as ageostrophic transports resulting from inertial effects, rather than numerical errors.

The right panels of Fig. 14 show the magnitude of the coherence between $\theta - \theta_o$ and θ_Q, θ_{loc}, and $\theta_{loc} + \theta_g$ in each region. The time series of $\theta - \theta_o$ and θ_{loc} are highly coherent on all time scales in the subtropical gyre. In contrast, the coherence between $\theta - \theta_o$ and θ_{loc} abruptly decreases for periods longer than 1–2 yr in the Gulf Stream region and subpolar gyre, indicating the importance of ocean dynamics (primarily θ_g in the Gulf Stream region and $\theta_{diff} + \theta_{bol}$ in the subpolar gyre).
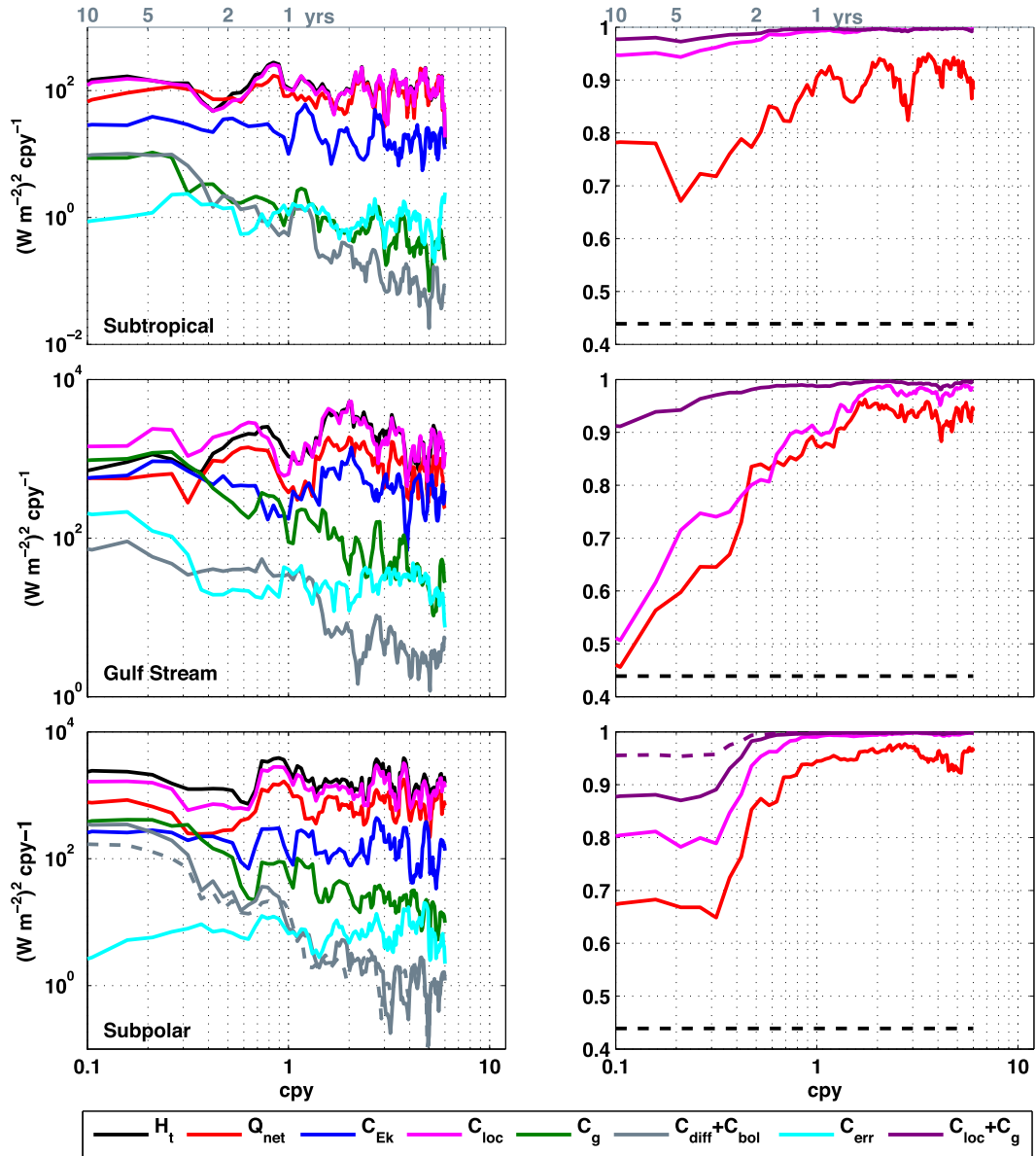
FIG. 12. (left) Power spectra of terms in H_t budget in (top) the interior of the subtropical gyre, (middle) the Gulf Stream region, and (bottom) the interior of the subpolar gyre. Dashed gray line in the bottom-left panel shows $C_{\text{diff}} + C_{\text{bol}}$ in the subpolar gyre for budgets integrated over D^* rather than D. Differences are primarily attributable to a reduction in C_{diff} (not shown). (right) Magnitude of the coherence between H_t and Q_{net}, C_{loc}, and $C_{\text{loc}} + C_g$ for (top) interior of the subtropical gyre, (middle) the Gulf Stream region, and (bottom) the interior of the subpolar gyre. The dashed black lines indicate the 95% confidence level. The phase is near zero everywhere and hence is not plotted. Purple dashed line shows the coherence between H_t and $C_{\text{loc}} + C_g$ for budgets integrated over D^*. Note the larger coherences on long time scales, demonstrating that $C_{\text{diff}} + C_{\text{bol}}$ plays a smaller role in budgets integrated over D^*.

In summary, the main results from the time series and coherences plotted in Fig. 14:

(i) In the interior of the subtropical gyre, θ_{loc} explains the majority of the variability of $\theta - \theta_o$ on all time scales (91% of the total variance of $\theta - \theta_o$ is explained by θ_{loc}).

(ii) In the Gulf Stream region, θ_g becomes important in setting $\theta - \theta_o$ for periods longer than about 1 yr and θ_g and θ_Q are highly anticorrelated (correlation is -0.90). These results suggest that on interannual time scales θ anomalies are formed by geostrophic heat transport convergence and damped by air–sea
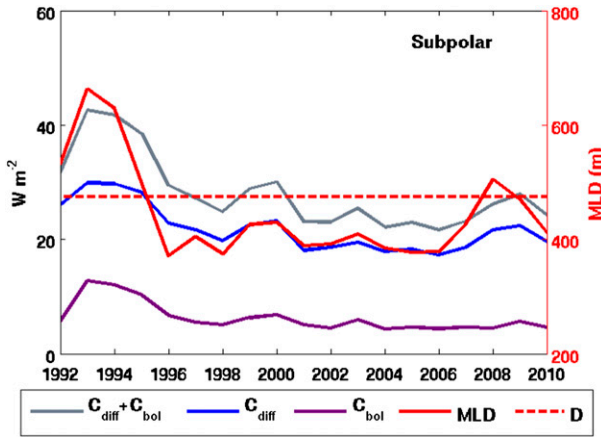
FIG. 13. Yearly average time series of C_{diff}, C_{bol}, and their sum in the subpolar gyre (left axis) are compared to a time series of the March MLD averaged over the subpolar gyre (right axis). The dashed red line shows D also averaged over the subpolar gyre. The C_{diff} and C_{bol} are highly correlated with March MLD (correlations of MLD with $C_{diff} = 0.82$ and $C_{bol} = 0.87$).

heat fluxes, but we acknowledge the difficulty of using correlations to imply causation.

(iii) In the subpolar gyre, θ_{diff} and θ_{bol} also contribute to variability of θ, particularly on the longest time scales resolved by the ECCO estimate. Here, θ_Q and $\theta_{bol} + \theta_{diff}$ are highly anticorrelated, particular at low frequencies (correlation is -0.82).

Computing budgets over D^* instead of D leads to no significant changes over the subtropical gyre and Gulf Stream region and quantitative rather than qualitative changes over the subpolar gyre. As expected, the contribution of C_{diff} to H_t^* is smaller but not entirely negligible (see Fig. 12, bottom panels). Correlations between C_{diff} and March MLD are reduced from 0.82 (for D) to 0.57 (for D^*). Despite the smaller role of diffusive and bolus fluxes, $\theta_{diff} + \theta_{bol}$ still plays a role in the budget of H^* at the lowest frequencies resolved in the ECCO estimate (see Fig. 14, bottom right panel).

b. Time scales of variability

In this section we determine the dominant time scale of variability in each of the three regions defined in Fig. 11a. Furthermore, we discuss how our analysis of the terms that contribute to H variability (section 5a) provides insight into the reason for the different dominant time scales of variability in each region.

Since the power spectra of H in each region are red at high frequencies and flatten out at low frequencies (see Figs. 11d,f,h), we fit a model of the form

$$P(f) = \frac{A}{f^n + \lambda^2} \qquad (10)$$

to the spectra $P(f)$, where f is frequency, n is the slope of the red portion of the spectrum, A determines the power level of the spectrum, and λ controls the frequency and period at which the spectrum flattens out. The dominant frequency [obtained by setting $\partial(fP)/\partial f = 0$; see Zangvil 1977] is

$$f^* = \left(\frac{\lambda^2}{n-1}\right)^{1/n}. \qquad (11)$$

We solve for n by finding the slope of the linear fit to $x = \ln f$ and $y = \ln P(f)$ for the red portion of the spectrum ($f > 0.5$ cpy) and then use a nonlinear fit to solve for A and λ. Values of n, λ, and $\tau \equiv 1/f^*$ in each region are given in Table 1. We find that $n = 2$ in the subtropical gyre and Gulf Stream region and $n > 2$ in the subpolar gyre, indicating that the subpolar gyre has relatively more variance at low frequencies and less variance at high frequencies than the other two regions. The dominant time scale τ is shortest in the subtropical gyre and longest in the subpolar gyre. Values of τ found via our fit are quite similar to the time scale of the peak on a variance conserving power spectra [plot of $\{\ln f, fP(f)\}$; not shown].

As discussed in section 5a, the majority of the H variance in the subtropical interior can be explained by local (air–sea heat flux and Ekman) forcing. This result suggests that H anomalies can be modeled by a first-order autoregressive process,

$$\frac{\partial H}{\partial t} = F_T - \lambda H, \qquad (12)$$

where F_T is the atmospheric forcing anomaly (taken to be white noise with power level A) and $\lambda > 0$ parameterizes feedback and damping processes (see, e.g., Frankignoul and Hasselmann 1977; Frankignoul 1981). In Frankignoul (1981) λ^{-1} is the damping time scale of SST anomalies, whereas in our case λ^{-1} is the effective damping time scale, which takes into account the enhanced persistence attributable to reemergence of SST anomalies (Deser et al. 2003; de Coëtlogon and Frankignoul 2003), as discussed in the Introduction. The power spectrum of H resulting from Eq. (12) is given by setting $n = 2$ in Eq. (10), and the time scale with maximum variance is $\tau = \lambda^{-1}$. Hence, the fact that we find $n = 2$ when we fit Eq. (10) to the power spectrum of H confirms that Eq. (12) is a realistic model of H variability in the subtropical gyre.

We can utilize our estimate of τ in the subtropical gyre to estimate the damping parameter (see Frankignoul et al. 1998),
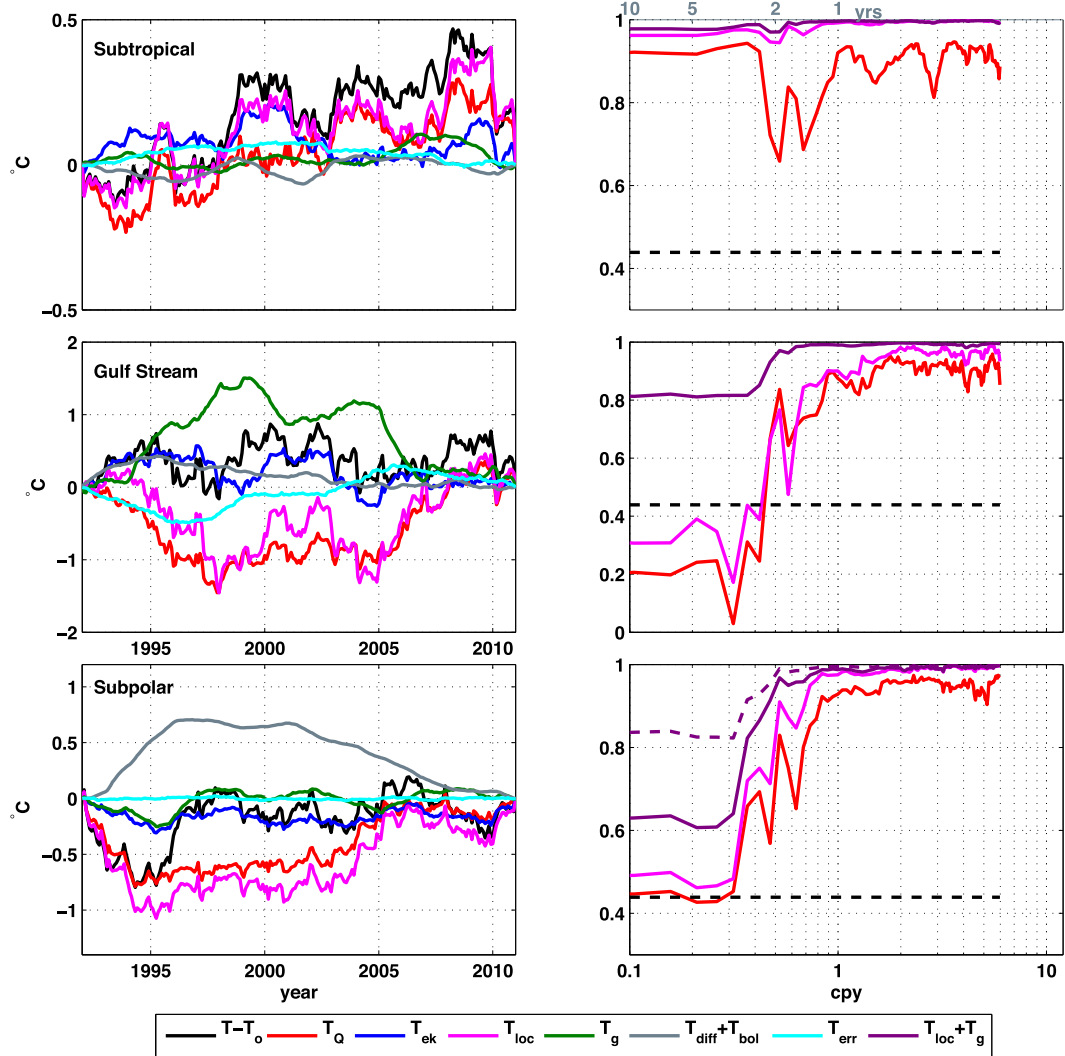
FIG. 14. (left) Time series of the terms in the θ budget over (top) the interior of the subtropical gyre, (middle) the Gulf Stream region, and (bottom) the interior of the subpolar gyre. (right) Magnitude of the coherence between $\theta - \theta_o$ and θ_Q, θ_{loc}, and $\theta_{loc} + \theta_g$ for (top) interior of the subtropical gyre, (middle) the Gulf Stream region, and (bottom) the interior of the subpolar gyre. The dashed black lines indicate the 95% confidence level. The phase is near zero everywhere and hence is not plotted. The purple dashed line shows the coherence between $\theta - \theta_o$ and $\theta_{loc} + \theta_g$ for budgets integrated over D^*. Note the larger coherences on long time scales compared to coherences for budgets over D, demonstrating that $\theta_{diff} + \theta_{bol}$ plays a smaller role in budgets integrated over D^*.

$$\alpha = \frac{\rho_o C_p D_{st}}{\tau}, \tag{13}$$

where $D_{st} = 203$ m is D averaged over the subtropical gyre. In the classic Frankignoul and Hasselmann (1977) model, α quantifies the magnitude of the air–sea heat flux response to SST anomalies. In our model, since H anomalies may be isolated beneath the seasonal thermocline during part of the year, α is a bulk measure of the damping of H anomalies (averaged over the course of the year and over depth D). We find that $\alpha = 11$ W m^{-2} K^{-1}, which is somewhat smaller than the canonical damping parameter of 20 W m^{-2} K^{-1} estimated

by Frankignoul et al. (1998). Our smaller value of α likely reflects the fact that H anomalies are isolated beneath the seasonal thermocline during the summer months and are thus not damped by air–sea heat fluxes.

TABLE 1. Values of n and τ in each region obtained by fitting Eq. (10) to spectra of H in each region.

Region	n	λ (cpy)	τ (yr)	τ (yr; 95% confidence)
Subtropical	2.0	0.43	2.4	2.2–2.6
Gulf Stream	2.0	0.30	3.3	3.0–3.8
Subpolar	2.4	0.17	5.2	4.9–5.7

[The impact of allowing α to vary seasonally is discussed in Deser et al. (2003).] However, as demonstrated by Frankignoul and Kestenare (2002), in the North Atlantic α ranges between 10 and 35 $\mathrm{W\,m^{-2}\,K^{-1}}$, so differences in α could also reflect averaging over a different geographical area (the subtropical gyre in our case and the entire North Atlantic in Frankignoul et al. 1998). It is also important to point out that Frankignoul et al. (1998) and Frankignoul and Kestenare (2002) estimate α via lagged covariances between SST and air–sea heat flux observations, whereas we have simply estimated the value to α that is consistent with the observed values of D_{st} and τ.

Variability of H in the Gulf Stream region appears to be forced by geostrophic heat transport convergences and damped by air–sea heat fluxes. Thus, ocean dynamics play a role in setting the dominant time scale and hence the predictability of H anomalies (and likely SST anomalies as well) over the Gulf Stream region. While we have not explored the dynamics responsible for these geostrophic heat transport convergence anomalies in detail, one possible hypothesis is that changes in the Gulf Stream path are the result of stochastic atmospheric forcing integrated over Rossby wave characteristics (Frankignoul et al. 1997; Marshall et al. 2001a; Piecuch and Ponte 2012a). The theoretically predicted baroclinic pressure spectrum for stochastically forced Rossby waves has a slope of -2 at high frequencies and flattens out at low frequencies (longer than the Rossby wave crossing time scale) to a level that increases quadratically with distance from the eastern boundary. [See Eq. (16) in Frankignoul et al. (1997) for the full equation for the spectrum.] The fact that we find $n = 2$ supports the hypothesis that wind forced baroclinic Rossby waves play a role in setting geostrophic transports and hence H variability in the Gulf Stream region. The value for τ of 3–4 yr is a bit shorter than the expected (decadal) Rossby wave crossing time at a latitude of approximately 40°N (Sturges et al. 1998; Marshall et al. 2001b; Wunsch and Heimbach 2009). However, 1) mean flows and resulting potential vorticity gradients may act to increase the phase speed (Tulloch et al. 2009) and 2) much evidence suggests that, because of damping and instability (Isachsen et al. 2007), Rossby waves may reflect stochastic forcing over a more localized region (Osychny and Cornillon 2004). Addressing these questions is beyond the scope of this work, but in future work we plan to test if a linear Rossby wave model forced by observed wind (and perhaps buoyancy) forcing can explain the observed geostrophic variability in the Gulf Stream region.

Although local atmospheric forcing explains over 70% of the variance of H_t in the subpolar gyre, diffusion and bolus transports exhibit significant low-frequency variability and thus play a large role in the H budget in the subpolar gyre. Low-frequency variability of diffusive and bolus convergences is related to low-frequency variability of the wintertime MLD in the subpolar gyre. The steeper slope ($n > 2$) in the subpolar gyre is consistent with the dominance of slow processes, such as diffusion and mixing, which predominantly lead to variance at low frequencies.

6. Conclusions

This paper uses an ocean state estimate (ECCO) to quantify the upper-ocean heat budget in the North Atlantic on intraannual–interannual time scales. We introduce three novel techniques for viewing upper-ocean heat budgets:

(i) The heat budget is integrated over the maximum climatological mixed layer depth, which varies spatially. This method gives results that are relevant for explaining SST variability (on interannual time scales) while avoiding strong contributions from vertical diffusion and entrainment and thus simplifying the analysis.

(ii) Advective heat transport convergences are separated into Ekman and geostrophic convergences, a technique that is successful away from boundary regions.

(iii) Air–sea heat fluxes and Ekman advection are combined into one local forcing term.

The central result of our analysis is that over large swaths of the North Atlantic, including the subtropics and the subpolar gyre, the tendency of H is predominantly explained (>70% of variance) by local (air–sea heat flux and Ekman) forcing. In contrast, local air–sea heat fluxes (commonly used to determine the importance of local atmospheric forcing) alone explain only about 50% of the variance in these regions.

Based on the distinct dynamics of H variability, we separate the North Atlantic into three regions (the interior of the subtropical gyre, the Gulf Stream, and the interior of the subpolar gyre) and present a detailed analysis of the terms that are important in the H budget on various time scales. Results from our regional analysis are presented in two distinct and complementary ways: 1) consideration of fluxes contributing to H_t and 2) temporally integrated budgets of H. We find the following:

(i) In the interior of the subtropical gyre, local forcing explains the majority of the variance of both H_t and H on all time scales resolved by the ECCO estimate ($1/6 \leq \tau \leq 9.5\,\mathrm{yr}$).

(ii) In the Gulf Stream region, geostrophic heat transport convergences play an increasingly important role in the H_t budget on time scales longer than about $\frac{1}{2}$ yr. Analysis of temporally integrated budgets show that both changes in geostrophic convergences and local air–sea heat fluxes play a leading-order role in the H budget. Geostrophic convergences and air–sea heat fluxes are strongly anticorrelated, which is consistent with the hypothesis that at low frequencies H anomalies are forced by geostrophic convergences and damped by air–sea heat fluxes.

(iii) Geostrophic transports, diffusion, and bolus transports play a role in H_t variability on time scales longer than about 1 yr in the interior of the subpolar gyre. Annual average diffusive and bolus transports are highly correlated with variability in wintertime mixed layer depths. Temporally integrated budgets highlight the importance of diffusion and bolus transports, since these terms exhibit substantial low-frequency variability.

Our analysis is complementary to previous studies attempting to determine the processes that are important in setting SST and UOHC variability in the North Atlantic. In some sense our study bridges the gap between theoretical studies, such as the null hypothesis (Hasselmann 1976; Frankignoul and Hasselmann 1977) or Rossby wave models (Frankignoul et al. 1997; Marshall et al. 2001a), and numerical studies utilizing ocean data or GCM output. Here, we quantitatively test the null hypothesis to determine in what regions and on what time scales local atmospheric forcing can explain observed UOHC variability. We find that atmospheric (air–sea heat flux and Ekman) forcing can explain 91% of the variance of UOHC in the interior of the subtropical gyre on time scales resolved by ECCO (<9.5 yr). Additionally, our finding that geostrophic heat transport convergences are important for UOHC variability along the Gulf Stream path is consistent with the idea that variability on the western boundary is in part determined by Rossby wave dynamics (Frankignoul et al. 1997; Marshall et al. 2001a), although here we do not explicitly determine the origin of the geostrophic variability.

A complementary technique for understanding the relative roles of atmospheric forcing and ocean dynamics in setting SST and UOHC is to compare the SST and UOHC variability in an ocean mixed layer model to that of a fully coupled GCM. Using this technique Seager et al. (2000) argue that the majority of wintertime SST variability observed during the last four decades can be explained as a (local) passive response to atmospheric forcing. Their assessment regarding the importance of local atmospheric forcing is quite similar to our results. Their results differ from ours in that they find Ekman transports to be important only in the subpolar North Atlantic, whereas we find them to be important in the subtropics as well, and they do not isolate the Gulf Stream as a region where geostrophic advection is important.

It is not easy to compare our results directly to the numerous studies that consider numerical UOHC budgets because of the different definitions of UOHC and regions studied. For example, Grist et al. (2010) use an eddy-permitting ocean model to show that air–sea heat fluxes play only a minor role in setting the depth integrated heat content in the subtropical and subpolar North Atlantic but are comparable in magnitude to the advective heat transport convergence in the tropical North Atlantic. The dominant role of advective heat transport convergences compared to air–sea heat fluxes is likely the result of taking an integral over the full ocean depth rather than the near surface ocean. Our results are consistent with the findings of Dong and Kelly (2004) and Dong et al. (2007) that interannual UOHC anomalies (defined as the integral over the top 400 m) in the Gulf Stream region are forced by changes in ocean geostrophic advection and damped by air–sea heat fluxes.

A common statistical technique for assessing the relative roles of atmospheric forcing and ocean dynamics is computing correlations between winds/air–sea heat fluxes and SST on various time scales. Kushnir (1994) utilizes SST and sea level pressure data to argue that, while the atmosphere forces SST anomalies on interannual time scales, ocean dynamics plays a role in setting SST on decadal time scales. In contrast, Deser and Blackmon (1993) do not find a difference between the SST–wind relationship on different time scales and suggest that SST is the passive response to atmospheric forcing on all time scales resolved in their study (90 years of data). Gulev et al. (2013) utilize SST and air–sea heat flux estimates to argue that in the midlatitude North Atlantic (defined as 35°–50°N) surface turbulent heat fluxes are driven by the ocean and may force the atmosphere on time scales longer than 10 years. While our study does not resolve decadal time scales and thus cannot directly be compared to these results, our work highlights the fact that the time scale for which ocean dynamics becomes important in setting SST and UOHC depends strongly on the region considered. Our analysis also provides dynamical insight into the reason why dominant time scales of UOHC variability are different in each region. The dominant time scale of UOHC variability appears to be set by the damping time scale of UOHC anomalies in the subtropical gyre, geostrophic

variability (perhaps the time scale for Rossby waves to cross the basin) in the Gulf Stream region, and eddies and diffusive processes (likely related to deep convection and restratification) in the subpolar gyre.

REFERENCES

Alexander, M. A., and C. Deser, 1995: A mechanism for the recurrence of wintertime midlatitude SST anomalies. *J. Phys. Oceanogr.,* **25,** 122–137, doi:10.1175/1520-0485(1995)025<0122: AMFTRO>2.0.CO;2.

Barsugli, J. J., and D. S. Battisti, 1998: The basic effects of atmosphere–ocean thermal coupling on midlatitude variability. *J. Atmos. Sci.,* **55,** 477–493, doi:10.1175/1520-0469(1998)055<0477: TBEOAO>2.0.CO;2.

Bjerknes, J., 1964: Atlantic air–sea interaction. *Advances in Geophysics,* Vol. 10, Academic Press, 1–82, doi:10.1016/ S0065-2687(08)60005-9.

Buckley, M. W., D. Ferreira, J.-M. Campin, J. Marshall, and R. Tulloch, 2012: On the relationship between decadal buoyancy anomalies and variability of the atlantic meridional overturning circulation. *J. Climate,* **25,** 8009–8030, doi:10.1175/ JCLI-D-11-00505.1.

Campin, J.-M., A. Adcroft, C. Hill, and J. Marshall, 2004: Conservation of properties in a free-surface model. *Ocean Modell.,* **6,** 221–244, doi:10.1016/S1463-5003(03)00009-X.

Cayan, D. R., 1992a: Latent and sensible heat flux anomalies over the northern oceans: Driving the sea surface temperature. *J. Phys. Oceanogr.,* **22,** 859–881, doi:10.1175/1520-0485(1992)022<0859: LASHFA>2.0.CO;2.

——, 1992b: Latent and sensible heat flux anomalies over the northern oceans: The connection to monthly atmospheric circulation. *J. Climate,* **5,** 354–369, doi:10.1175/ 1520-0442(1992)005<0354:LASHFA>2.0.CO;2.

Cunningham, S. A., and Coauthors, 2007: Temporal variability of the Atlantic meridional overturning circulation at 26.5°N. *Science,* **317,** 935–937, doi:10.1126/science.1141304.

Czaja, A., and J. Marshall, 2001: Observations of atmosphere-ocean coupling in the North Atlantic. *Quart. J. Roy. Meteor. Soc.,* **127,** 1893–1916, doi:10.1002/qj.49712757603.

de Boyer Montégut, C., G. Madec, A. S. Fischer, A. Lazar, and D. Iudicone, 2004: Mixed layer depth over the global ocean: An examination of profile data and a profile-based climatology. *J. Geophys. Res.,* **109,** C12003, doi:10.1029/2004JC002378.

de Coëtlogon, G., and C. Frankignoul, 2003: The persistence of winter sea surface temperature in the North Atlantic. *J. Climate,* **16,** 1364–1377, doi:10.1175/1520-0442-16.9.1364.

Deser, C., and M. L. Blackmon, 1993: Surface climate variations over the North Atlantic Ocean during winter: 1900–1989. *J. Climate,* **6,** 1743–1753, doi:10.1175/1520-0442(1993)006<1743: SCVOTN>2.0.CO;2.

——, M. A. Alexander, and M. S. Timlin, 2003: Understanding the persistence of sea surface temperature anomalies in midlatitudes. *J. Climate,* **16,** 57–72, doi:10.1175/ 1520-0442(2003)016<0057:UTPOSS>2.0.CO;2.

Doney, S. C., S. Yeager, G. Danabasoglu, W. G. Large, and J. C. McWilliams, 2007: Mechanisms governing interannual variability of upper-ocean temperature in a global ocean hindcast simulation. *J. Phys. Oceanogr.,* **37,** 1918–1938, doi:10.1175/ JPO3089.1.

Dong, S., and K. A. Kelly, 2004: Heat budget in the Gulf Stream region: The importance of heat storage and advection. *J. Phys. Oceanogr.,* **34,** 1214–1231, doi:10.1175/1520-0485(2004)034<1214: HBITGS>2.0.CO;2.

——, S. L. Hautala, and K. A. Kelly, 2007: Interannual variations in upper-ocean heat content and heat transport convergence in the western North Atlantic. *J. Phys. Oceanogr.,* **37,** 2682–2697, doi:10.1175/2007JPO3645.1.

Fan, M., and E. K. Schneider, 2012: Observed decadal North Atlantic tripole SST variability. Part I: Weather noise forcing and coupled response. *J. Atmos. Sci.,* **69,** 35–50, doi:10.1175/ JAS-D-11-018.1.

Foltz, G. R., and M. J. McPhaden, 2006: The role of oceanic heat advection in the evolution of tropical North and South Atlantic SST anomalies. *J. Climate,* **19,** 6122–6138, doi:10.1175/ JCLI3961.1.

——, S. A. Grodsky, J. A. Carton, and M. J. McPhaden, 2003: Seasonal mixed layer heat budget of the tropical Atlantic Ocean. *Geophys. Res. Lett.,* **108,** 3146, doi:10.1029/ 2002JC001584.

——, C. Schmid, and R. Lumpkin, 2013: Seasonal cycle of the mixed layer heat budget in the northeastern tropical Atlantic Ocean. *J. Climate,* **26,** 8169–8188, doi:10.1175/ JCLI-D-13-00037.1.

Forget, G., 2010: Mapping ocean observations in a dynamical framework: A 2004–06 ocean atlas. *J. Phys. Oceanogr.,* **40,** 1201–1221, doi:10.1175/2009JPO4043.1.

——, and C. Wunsch, 2007: Estimated global hydrographic variability. *J. Phys. Oceanogr.,* **37,** 1997–2008, doi:10.1175/JPO3072.1.

——, B. Ferron, and H. Mercier, 2008a: Combining Argo profiles with a general circulation model in the North Atlantic. Part 1: Estimation of hydrographic and circulation anomalies from synthetic profiles, over a year. *Ocean Modell.,* **20,** 1–16, doi:10.1016/j.ocemod.2007.06.001.

——, H. Mercier, and B. Ferron, 2008b: Combining Argo profiles with a general circulation model in the North Atlantic. Part 2: Realistic transports and improved hydrography, between spring 2002 and spring 2003. *Ocean Modell.,* **20,** 17–34, doi:10.1016/j.ocemod.2007.06.002.

——, G. Maze, M. Buckley, and J. Marshall, 2011: Estimated seasonal cycle of North Atlantic Eighteen Degree Water volume. *J. Phys. Oceanogr.,* **41,** 269–286, doi:10.1175/2010JPO4257.1.

Frankignoul, C., 1981: Low-frequency temperature fluctuations off Bermuda. *J. Geophys. Res.,* **86,** 6522–6528, doi:10.1029/ JC086iC07p06522.

——, 1985: Sea surface temperature anomalies, planetary waves, and air-sea feedback in the middle latitudes. *Rev. Geophys.,* **23,** 357–390, doi:10.1029/RG023i004p00357.

——, and K. Hasselmann, 1977: Stochastic climate models, part II: Application to sea-surface temperature anomalies and thermocline variability. *Tellus,* **29,** 289–305, doi:10.1111/ j.2153-3490.1977.tb00740.x.

——, and R. W. Reynolds, 1983: Testing a dynamical model for mid-latitude sea surface temperature anomalies. *J. Phys. Oceanogr.,* **13,** 1131–1145, doi:10.1175/1520-0485(1983)013<1131: TADMFM>2.0.CO;2.

——, and E. E. Kestenare, 2002: The surface heat flux feedback. Part I: Estimates from observations in the Atlantic and the North Pacific. *Climate Dyn.,* **19,** 633–647, doi:10.1007/s00382-002-0252-x.

——, P. Müller, and E. Zorita, 1997: A simple model of the decadal response of the ocean to stochastic wind forcing. *J. Phys. Oceanogr.,* **27,** 1533–1546, doi:10.1175/1520-0485(1997)027<1533: ASMOTD>2.0.CO;2.

——, A. Czaja, and B. L'Heveder, 1998: Air–sea feedback in the North Atlantic and surface boundary conditions for ocean models. *J. Climate,* **11,** 2310–2324, doi:10.1175/ 1520-0442(1998)011<2310:ASFITN>2.0.CO;2.

Gaspar, P., Y. Grégoris, and J.-M. Lefevre, 1990: A simple eddy kinetic energy model for simulations of the oceanic vertical mixing: Tests at station Papa and long-term upper ocean study site. *J. Geophys. Res.,* **95** (C9), 16 179–16 193, doi:10.1029/ JC095iC09p16179.

Gent, P. R., and J. C. McWilliams, 1990: Isopycnal mixing in ocean circulation models. *J. Phys. Oceanogr.,* **20,** 150–155, doi:10.1175/1520-0485(1990)020<0150:IMIOCM>2.0.CO;2.

Grist, J. P., and Coauthors, 2010: The roles of surface heat flux and ocean heat transport convergence in determining Atlantic Ocean temperature variability. *Ocean Dyn.,* **60,** 771–790, doi:10.1007/s10236-010-0292-4.

Gulev, S. K., M. Latif, N. Keenlyside, W. Park, and K. P. Koltermann, 2013: North Atlantic Ocean control on surface heat flux on multidecadal timescales. *Nature,* **499,** 464–467, doi:10.1038/ nature12268.

Hasselmann, K., 1976: Stochastic climate models, part I: Theory. *Tellus,* **6,** 472–485.

Isachsen, P. E., J. H. LaCasce, and J. Pedlosky, 2007: Rossby wave instability and apparent phase speeds in large ocean basins. *J. Phys. Oceanogr.,* **37,** 1177–1191, doi:10.1175/JPO3054.1.

Jayne, S. R., and J. Marotzke, 2001: The dynamics of ocean heat transport variability. *Rev. Geophys.,* **39,** 385–411, doi:10.1029/ 2000RG000084.

Johns, W. E., and Coauthors, 2011: Continuous, array-based estimates of Atlantic Ocean heat transport at 26.5°N. *J. Climate,* **24,** 2429–2449, doi:10.1175/2010JCLI3997.1.

Johnson, H. L., and D. P. Marshall, 2002: A theory for the surface Atlantic response to thermohaline variability. *J. Phys. Oceanogr.,* **32,** 1121–1132, doi:10.1175/1520-0485(2002)032<1121: ATFTSA>2.0.CO;2.

Kara, A. B., P. A. Rochford, and H. E. Hurlburt, 2000: An optimal definition for ocean mixed layer depth. *J. Geophys. Res.,* **105** (C7), 16 803–16 821, doi:10.1029/2000JC900072.

——, ——, and ——, 2002: Naval Research Laboratory mixed layer depth (NMLD) climatologies. Naval Research Laboratory Tech. Rep. NRL/FR/ 7330–02-9995, 26 pp.

Keenlyside, N., M. Latif, J. Jungclaus, L. Kornblueh, and E. Roeckner, 2008: Advancing decadal-scale climate prediction in the North Atlantic sector. *Nature,* **453,** 84–88, doi:10.1038/ nature06921.

Kim, S.-B., I. Fukumori, and T. Lee, 2006: The closure of the ocean mixed layer temperature budget using level-coordinate model fields. *J. Atmos. Oceanic Technol.,* **23,** 840–853, doi:10.1175/ JTECH1883.1.

Knight, J. R., C. K. Folland, and A. A. Scaife, 2006: Climate impacts of the Atlantic multidecadal oscillation. *Geophys. Res. Lett.,* **33,** L17706, doi:10.1029/2006GL026242.

Kushnir, Y., 1994: Interdecadal variations in North Atlantic sea surface temperature and associated atmospheric conditions. *J. Climate,* **7,** 141–157, doi:10.1175/1520-0442(1994)007<0141: IVINAS>2.0.CO;2.

——, W. A. Robinson, I. Bladé, N. M. J. Hall, S. Peng, and R. Sutton, 2002: Atmospheric GCM response to extratropical SST anomalies: Synthesis and evaluation. *J. Climate,* **15,** 2233–2256, doi:10.1175/1520-0442(2002)015<2233: AGRTES>2.0.CO;2.

Levitus, S., 1987: Meridional Ekman heat fluxes for the world ocean and individual ocean basins. *J. Phys. Oceanogr.,* **17,** 1484–1492, doi:10.1175/1520-0485(1987)017<1484:MEHFFT>2.0.CO;2.

Losch, M., D. Menemenlis, J. Campin, P. Heimbach, and C. Hill, 2010: On the formulation of sea-ice models. Part 1: Effects of different solver implementations and parameterizations. *Ocean Modell.,* **33** (1–2), 129–144, doi:10.1016/ j.ocemod.2009.12.008.

Marshall, J., H. Johnson, and J. Goodman, 2001a: A study of the interaction of the North Atlantic Oscillation with ocean circulation. *J. Climate,* **14,** 1399–1421, doi:10.1175/ 1520-0442(2001)014<1399:ASOTIO>2.0.CO;2.

——, and Coauthors, 2001b: North Atlantic climate variability: Phenomena, impacts and mechanisms. *Int. J. Climatol.,* **21,** 1863–1898, doi:10.1002/joc.693.

Namias, J., and R. M. Born, 1970: Temporal coherence in North Pacific sea-surface temperature patterns. *J. Geophys. Res.,* **75,** 5952–5955, doi:10.1029/JC075i030p05952.

Niiler, P., and E. Kraus, 1977: One-dimensional models of the upper ocean. *Modeling and Prediction of the Upper Layers of the Ocean,* E. Kraus, Ed., Pergamon, 143–172.

Osychny, V., and P. Cornillon, 2004: Properties of Rossby waves in the North Atlantic estimated from satellite data. *J. Phys. Oceanogr.,* **34,** 61–76, doi:10.1175/1520-0485(2004)034<0061: PORWIT>2.0.CO;2.

Piecuch, C. G., and R. M. Ponte, 2012a: Buoyancy-driven interannual sea level changes in the southeast tropical Pacific. *Geophys. Res. Lett.,* **39,** L05607, doi:10.1029/2012GL051130.

——, and ——, 2012b: Importance of circulation changes to Atlantic heat storage rates. *J. Climate,* **25,** 350–362, doi:10.1175/ JCLI-D-11-00123.1.

Pohlmann, H., F. Sienz, and M. Latif, 2006: Influence of the multidecadal Atlantic meridional overturning circulation variability on European climate. *J. Climate,* **19,** 6062–6067, doi:10.1175/ JCLI3941.1.

Redi, M. H., 1982: Oceanic isopycnal mixing by coordinate rotation. *J. Phys. Oceanogr.,* **12,** 1154–1158, doi:10.1175/ 1520-0485(1982)012<1154:OIMBCR>2.0.CO;2.

Reynolds, R. W., N. A. Rayner, T. M. Smith, D. C. Stokes, and W. Wang, 2002: An improved in situ and satellite SST analysis for climate. *J. Climate,* **15,** 1609–1625, doi:10.1175/ 1520-0442(2002)015<1609:AIISAS>2.0.CO;2.

Schneider, E. K., and M. Fan, 2012: Observed decadal North Atlantic tripole SST variability. Part II: Diagnosis of mechanisms. *J. Atmos. Sci.,* **69,** 51–64, doi:10.1175/JAS-D-11-019.1.

Seager, R., Y. Kushnir, M. Visbeck, N. Naik, J. Miller, G. Krahmann, and H. Cullen, 2000: Causes of Atlantic Ocean climate variability between 1958 and 1998. *J. Climate,* **13,** 2845–2862, doi:10.1175/ 1520-0442(2000)013<2845:COAOCV>2.0.CO;2.

Smith, K. S., 2007: The geography of linear baroclinic instability in the Earth's oceans. *J. Mar. Res.,* **65,** 655–683, doi:10.1357/ 002224007783649484.

Speer, K., and G. Forget, 2013: Global distribution and formation of mode waters. *Ocean Circulation and Climate: A 21st*

Century Perspective, G. Siedler et al. Eds., Academic Press, 211–226.

Sturges, W., B. G. Hong, and A. J. Clarke, 1998: Decadal wind forcing of the North Atlantic subtropical gyre. *J. Phys. Oceanogr.,* **28,** 659–668, doi:10.1175/1520-0485(1998)028<0659:DWFOTN>2.0.CO;2.

Sutton, R. T., and D. L. R. Hodson, 2005: Atlantic Ocean forcing of North American and European summer climate. *Science,* **309,** 115–118, doi:10.1126/science.1109496.

Tulloch, R., and J. Marshall, 2012: Diagnosis of variability and predictability in the NCAR CCSM3 and GFDL CM2.1 coupled climate models. *J. Climate,* **25,** 4067–4080, doi:10.1175/JCLI-D-11-00460.1.

——, ——, and K. S. Smith, 2009: Interpretation of the propagation of surface altimetric observations in terms of planetary waves and gesotrophic turbulence. *J. Geophys. Res.,* **114,** C02005, doi:10.1029/2008JC005055.

Wunsch, C., and P. Heimbach, 2007: Practical global ocean state estimation. *Physica D,* **230,** 197–208, doi:10.1016/j.physd.2006.09.040.

——, and ——, 2009: The global zonally integrated ocean circulation, 1992–2006: Seasonal and decadal variability. *J. Phys. Oceanogr.,* **39,** 351–368, doi:10.1175/2008JPO4012.1.

——, and ——, 2013a: Dynamically and kinematically consistent global ocean circulation and ice state estimates. *Ocean Circulation and Climate: A 21st Century Perspective,* G. Siedler et al. Eds., Academic Press, 553–580.

——, and ——, 2013b: Two decades of the Atlantic meridional overturning circulation: Anatomy, variations, extremes, prediction, and overcoming its limitations. *J. Climate,* **26,** 7167–7186, doi:10.1175/JCLI-D-12-00478.1.

——, ——, R. M. Ponte, and I. Fukumori, 2009: The global general circulation of the ocean estimated by the ECCO consortium. *Oceanography,* **22,** 88–103, doi:10.5670/oceanog.2009.41.

Zangvil, A., 1977: On the presentation and interpretation of spectra of large-scale disturbances. *Mon. Wea. Rev.,* **105,** 1469–1472, doi:10.1175/1520-0493(1977)105<1469:OTPAIO>2.0.CO;2.

Zhang, R., and T. L. Delworth, 2006: Impact of Atlantic multidecadal oscillations on India/Sahel rainfall and Atlantic hurricanes. *Geophys. Res. Lett.,* **33,** L17712, doi:10.1029/2006GL026267.